The Astrophysical Journal, 837:97 (24pp), 2017 March 1 doi:10.3847/1538-4357/837/1/97

The Frontier Fields: Survey Design and Initial Results

J. M. Lotz[1], A. Koekemoer[1], D. Coe[2], N. Grogin[1], P. Capak[2], J. Mack[1], J. Anderson[1], R. Avila[1], E. A. Barker[1], D. Borncamp[1], G. Brammer[2], M. Durbin[1], H. Gunning[1], B. Hilbert[1], H. Jenkner[1], H. Khandrika[1], Z. Levay[1], R. A. Lucas[1], J. MacKenty[1], S. Ogaz[1], B. Porterfield[1], N. Reid[1], M. Robberto[1], P. Royle[1], L. J. Smith[2], L. J. Storrie-Lombardi[3], B. Sunnquist[1], J. Surace[3], D. C. Taylor[1], R. Williams[1], J. Bullock[4], M. Dickinson[5], S. Finkelstein[6], P. Natarajan[7], J. Richard[8], B. Robertson[9], J. Tumlinson[1], A. Zitrin[10], K. Flanagan[1], K. Sembach[1], B. T. Soifer[2], and M. Mountain[1]
[1] Space Telescope Science Institute, 3700 San Martin Drive, Baltimore, MD 21218, USA; lotz@stsci.edu
[2] European Space Agency/Space Telescope Science Institute, 3700 Sam Martin Drive, Baltimore, MD 21218, USA
[3] Spitzer Science Center, California Institute of Technology, Pasadena, CA 91106, USA
[4] Physics & Astronomy Department, University of California, Irvine, CA 92697, USA
[5] National Optical Astronomy Observatory, Tucson, AZ 85719, USA
[6] Department of Astronomy, University of Texas, Austin, TX 78712, USA
[7] Department of Astronomy, Yale University, New Haven, CT 06520, USA
[8] Univ. Lyon, Univ. Lyon1, Ens de Lyon, CNRS, Centre de Recherche Astrophysique de Lyon UMR5574, F-69230 Saint-Genis-Laval, France
[9] Department of Astronomy & Astrophysics, University of California, Santa Cruz, CA 95064, USA
[10] Department of Astronomy, California Institute of Technology, Pasadena, CA 92697, USA
Received 2016 May 19; revised 2016 October 19; accepted 2016 October 26; published 2017 March 7

Abstract

What are the faintest distant galaxies we can see with the *Hubble Space Telescope* (*HST*) now, before the launch of the *James Webb Space Telescope*? This is the challenge taken up by the Frontier Fields, a Director's discretionary time campaign with *HST* and the *Spitzer Space Telescope* to see deeper into the universe than ever before. The Frontier Fields combines the power of *HST* and *Spitzer* with the natural gravitational telescopes of massive high-magnification clusters of galaxies to produce the deepest observations of clusters and their lensed galaxies ever obtained. Six clusters—Abell 2744, MACSJ0416.1-2403, MACSJ0717.5+3745, MACSJ1149.5+2223, Abell S1063, and Abell 370—have been targeted by the *HST* ACS/WFC and WFC3/IR cameras with coordinated parallel fields for over 840 *HST* orbits. The parallel fields are the second-deepest observations thus far by *HST* with 5σ point-source depths of ∼29th ABmag. Galaxies behind the clusters experience typical magnification factors of a few, with small regions magnified by factors of 10–100. Therefore, the Frontier Field cluster *HST* images achieve intrinsic depths of ∼30–33 mag over very small volumes. *Spitzer* has obtained over 1000 hr of Director's discretionary imaging of the Frontier Field cluster and parallels in IRAC 3.6 and 4.5 μm bands to 5σ point-source depths of ∼26.5, 26.0 ABmag. We demonstrate the exceptional sensitivity of the *HST* Frontier Field images to faint high-redshift galaxies, and review the initial results related to the primary science goals.

Key words: cosmology: observations – galaxies: clusters: general – galaxies: high-redshift

1. Introduction

Exceptionally deep observations of the distant universe with the *Hubble Space Telescope* (*HST*) have consistently pushed the frontiers of human knowledge. A succession of observing programs with each generation of *HST* detectors, in concert with the other NASA Great Observatories (*Spitzer Space Telescope* and *Chandra X-ray Observatory*), have probed the star formation and assembly histories of galaxies through more than 95% of the universe's lifetime. These observations have been made publicly available to the greater astronomy community, enabling a wide range of science and ancillary observing programs. The study of *HST* deep fields has established a number of techniques now standard in extra-galactic astronomy, including the Lyman break selection of distant star-forming galaxies; photometric redshift determinations; stellar population fitting to multi-band photometry; quantitative morphological analysis; and the detection of high-redshift transient phenomena. Here we present the new Frontier Fields, an *HST* and *Spitzer* Director's discretionary time campaign to observe six massive strong-lensing clusters and six parallel fields, designed to simultaneously detect the faintest galaxies ever observed and provide a statistical picture of galaxy evolution at early times.

The first Hubble Deep Field (HDF) observations with *HST* WFPC2 revealed thousands of galaxies to 28th magnitude, fainter than any seen before (Williams et al. 1996; Ferguson et al. 2000). Utilizing the Lyman break technique (Guhathakurta et al. 1990; Songaila et al. 1990), the HDF and subsequent HDF-South (HDF-S; Casertano et al. 2000; Ferguson et al. 2000; Williams et al. 2000) detected significant numbers of distant star-forming galaxies visible in the optical out to redshifts $z \sim 5$ (e.g., Madau et al. 1996). *HST*'s deep images with high spatial resolution showed that many of these distant galaxies were smaller with higher surface brightnesses and more irregular structures than local galaxy populations (e.g., Abraham et al. 1996).

Follow-up observations of the HDF and HDF-S in the infrared with *HST*'s NICMOS camera (Dickinson 1999; Thompson et al. 1999; Franx 2003) enabled studies of the stellar mass of the $z < 5$ populations (e.g., Papovich et al. 2001; Dickinson et al. 2003; Fontana et al. 2003) as well as the detection of higher redshift galaxies at $5 < z < 7$ (Bouwens et al. 2003; Thompson 2003) and intrinsically redder populations (Fernández-Soto et al. 1999; Stiavelli et al. 1999; Labbé et al. 2003). Combined with the spectroscopic confirmation of many of these faint galaxies (e.g., Steidel et al. 1996; Lowenthal et al. 1997; Cohen et al. 2000), it

became possible to track the cosmic star formation (Madau et al. 1996; Lanzetta et al. 2002; Bouwens et al. 2003) and assembly history of stellar mass (Dickinson et al. 2003) over the majority of the universe's lifetime. *HST* NICMOS observations of the HDF in 1997 discovered the highest redshift supernova (SN) of Type Ia known at that time ($z = 1.7$), confirming the acceleration of the universe (Riess et al. 2001).

After the original HDFs, synergistic multi-wavelength deep observations with Great Observatories and new capabilities on the *HST* further expanded the boundaries of our understanding. The installation of the Advanced Camera for Surveys Wide Field Camera (ACS/WFC; Ford et al. 1998) on *HST* in 2002 greatly improved the depth and area of optical imaging possible within a fixed exposure time. The fields for the Great Observatories Origins Deep Survey (GOODS; Giavalisco et al. 2004) were chosen to overlap with existing X-ray deep fields from *Chandra* (HDF/*Chandra* Deep Field North and the new *Chandra* Deep Field South (CDFS); Hornschemeier et al. 2000; Giacconi et al. 2001). New *HST* and *Spitzer* imaging produced high-quality and deep multi-wavelength photometry, revealed new distant galaxy populations, measured photometric redshifts, improved stellar mass estimates, and could be matched to faint X-ray sources in the *Chandra* Deep Fields (e.g., Mobasher et al. 2004; Treister et al. 2004; Barger et al. 2005; Fontana et al. 2006; Grazian et al. 2006; Pope et al. 2006). The cadence of the *HST* GOODS observations was designed to perform a systematic search for high-redshift supernovae (Riess et al. 2004a, 2004b). The location of the *HST* Ultra Deep Field (HUDF; Beckwith et al. 2006) within GOODS-S/CDFS was chosen to leverage this existing data with an additional 400 orbits (268 hr) to reach optical depths of ~29th magnitude, fainter than original HDF WFPC2 limits. Deep NICMOS IR imaging was also obtained in the HUDF (Thompson et al. 2005). The resulting "wedding cake" survey of the combined GOODS and HUDF observations proved to be an important strategy for spanning the depth and area needed to constrain both the bright and faint ends of the luminosity function of galaxies approaching the epoch of reionization (e.g., Bouwens et al. 2007).

With the success of the *HST* servicing mission SM4 in 2009 and the installation of the Wide Field Camera 3 (WFC3; MacKenty et al. 2008) with its IR channel, *HST* greatly improved the efficiency of its high-spatial-resolution near-infrared imaging. The WFC3 Early Release Science near-infrared observations of GOODS-S (Windhorst et al. 2011) and deep imaging in HUDF and parallels revealed new populations of galaxies at $z \sim 8$ (Bouwens et al. 2010; Illingworth & Bouwens 2010). The UDF 2012 WFC3/IR campaign (Ellis et al. 2013; Koekemoer et al. 2013) added the F140W filter and deeper observations in F105W and F160W filters to increase the detection efficiency of highest redshift candidates ($8.5 < z < 12$) to ~30th magnitude. (See also Illingworth et al. 2013 for a separate reduction of all HUDF data.) Wider field near-infrared imaging with the *HST* Multi-Cycle Treasury Cosmic Assembly Near-infrared Deep Extra-galactic Legacy Survey (CANDELS; Grogin et al. 2012; Koekemoer et al. 2011) built upon the previous *HST* ACS/WFC and *Spitzer* observations of the GOODS, GEMS (Rix et al. 2004), COSMOS (Scoville et al. 2007), EGS (Davis et al. 2007), and UDS (Lawrence et al. 2007) extragalactic legacy fields. Thanks to WFC3, detections of $z \sim 8$ candidates are now relatively commonplace (e.g., Finkelstein et al. 2010; Labbé et al. 2010; McLure et al. 2011; Yan et al. 2011; Bradley et al. 2012). The current measurement of the cosmic star formation history extends to less than 500 Myr after the Big Bang (e.g., Ellis et al. 2013; Oesch et al. 2013, 2016; Bouwens et al. 2015a; Finkelstein et al. 2015; but see Brammer et al. 2013; Pirzkal et al. 2013), albeit with very small numbers of candidates at $z > 9$. *HST*'s observations of high-redshift galaxies have placed important constraints on cosmological measures of reionization (e.g., Bouwens et al. 2015b; Finkelstein et al. 2015; Robertson et al. 2015).

With the launch of the *James Webb Space Telescope* (*JWST*) still several years away, and no new servicing missions to *HST* planned, significant progress on understanding the first billion years of the universe with the remaining years of *HST* poses a major challenge. The *HST* and *Spitzer* projects proposed supporting a new joint Deep Fields program supported with Director's discretionary time in their 2012 NASA Senior Review proposals. The Hubble Deep Fields Initiative science working group (HDFI SWG) was convened by STScI Director M. Mountain in 2012. They recommended a new strategy to "go deep": use massive clusters of galaxies as cosmic telescopes, combined with very deep *HST* and *Spitzer* observations.[11] Very massive clusters of galaxies are the most massive structures in the universe, bending spacetime to create efficient gravitational lenses (e.g., Kneib & Natarajan 2011). The light from galaxies behind these natural telescopes experiences magnification factors of a few within a few arcminutes of the cluster cores, and magnifications ~10 or greater within smaller windows along the critical curves. Therefore, *HST* observations of these strongly lensed fields can probe galaxies as intrinsically faint or fainter than those detected in the HUDF in a much shorter exposure time—provided those galaxies fall within the high-magnification windows.

The advantages of this strategy had already been demonstrated by the Cluster Lensing and Supernova Survey (CLASH; Postman et al. 2012), a 524-orbit *HST* Multi-Cycle Treasury Program to study the gravitational lensing properties of 25 galaxy clusters. CLASH targeted each cluster with shallow observations in 16 ultraviolet–near-infrared *HST* bandpasses, in order to obtain precise photometric redshift constraints on background lensed galaxies. Within only a few orbits of *HST* time in the reddest filters, CLASH discovered several $z > 9$ galaxy candidates highly magnified by intervening massive clusters at $z \sim 0.5$ (Zheng et al. 2012; Coe et al. 2013; Bouwens et al. 2014).

The Frontier Fields program is an ambitious multi-cycle observing campaign using Director's discretionary time with *HST* and *Spitzer Space Telescope* to peer deeper into the universe than ever before. The Frontier Fields combine the power of *HST* with the natural gravitational telescopes of six high-magnification clusters of galaxies to produce the deepest observations of clusters and their lensed galaxies ever obtained. The *HST* cluster images are obtained in parallel with six "blank" field images; the parallel field images are the second deepest images ever obtained, and triple the blank field area imaged to a depth of 29th ABmag. The *Spitzer Space Telescope* is also dedicating over 1000 hr of Director's discretionary time to obtain IRAC 3.6 and 4.5 μm imaging to

[11] www.stsci.edu/hst/campaigns/frontier-fields/documents/HDFI_SWGReport2012.pdf

depths of 26.5, 26.0 ABmag in the six cluster and six parallel Frontier Fields. In this paper, we describe the primary science goals in Section 2, the field selection criterion in Section 3, the Frontier Field clusters and parallel fields in Section 4, the *HST* and *Spitzer* observations in Section 5, and the public Frontier Fields lensing modeling effort in Section 6. In Section 7, we present the image depths achieved for the *HST* observations for the first two cluster and parallel fields, and review the current results relevant to primary science goals. Further details, the latest *HST* data releases, and Frontier Fields updates may be found at www.stsci.edu/hst/campaigns/frontier-fields/ and at the STScI MAST Archive (10.17909/T9KK5N). Details describing the *Spitzer* observations will be presented in P. Capak et al. (2017, in preparation) and more information is available at ssc.spitzer.caltech.edu/warmmission/scheduling/approvedprograms/ddt/frontier/.

2. Science Goals and Strategy

The primary science goals of the Frontier Fields are to explore the high-redshift universe accessible only with deep *HST* observations, and to set the scene for *JWST* studies of the early universe. Studies of high-redshift quasar absorption lines have found that the epoch of reionization was completed by $z \sim 6$ (Fan et al. 2006), while observations of the cosmic microwave background place the start of reionization before $z \sim 10$ (e.g., Spergel et al. 2003; Hinshaw et al. 2013; Planck Collaboration et al. 2016). Including recent estimates of the optical depth from *Planck* data, the era between $z \sim 11$ and $z \sim 6$ probed by the deepest and reddest *HST* observations marks a critical transition in the universe's history (e.g., Bouwens et al. 2015b; Mitra et al. 2015; Planck Collaboration et al. 2016; Robertson et al. 2015).

The installation of the *HST* WFC3 camera with the near-infrared channel dramatically increased the number of galaxy candidates detected at $z > 6$. However, prior to the start of the Frontier Fields in 2013, astronomers' understanding of the galaxy populations during the epoch of reionization was based largely on those detected in direct *HST* WFC3/IR imaging surveys (HUDF, CANDELS, BORG) and handfuls of lensed objects in shallow *HST* observations from CLASH. The detected unlensed galaxies are the most luminous objects of their era, and thus significantly more massive and rare than the progenitors of today's Milky Way galaxies (e.g., Behroozi et al. 2013; Boylan-Kolchin et al. 2014). High-redshift galaxies are barely resolved by *HST* (Oesch et al. 2010; Ono et al. 2013), with lensed $z > 8$ galaxies yielding intrinsic sizes less than a few hundred parsecs across (Coe et al. 2013). Because such high-redshift galaxies are often observable only in the reddest *HST* bandpasses, limited information about their rest-frame ultraviolet slopes, stellar populations, and dust content can be inferred from their observed colors (e.g., Bouwens et al. 2012; Finkelstein et al. 2012). Unseen $z > 6$ dwarf galaxies well below *HST*'s nominal direct detection limit are needed to produce the number of ionizing photons required to disassociate the universe's reservoir of intergalactic neutral hydrogen (e.g., Finkelstein et al. 2015; Robertson et al. 2015). Very few candidates at $z \sim 9$ and above were identified (Zheng et al. 2012; Coe et al. 2013; Ellis et al. 2013; Oesch et al. 2013), resulting in vigorous debate about how quickly the first star formation proceeded and how many $z > 9$ objects future *JWST* observations might see (Oesch et al. 2012). (The role of early black holes in terms of their contribution to the reionization budget is currently unknown and this will be revealed by *JWST*.)

In order to address many of these unknowns, the Frontier Fields program was designed with the following science aims:

1. To reveal populations of $z = 5$–10 galaxies that are >10 times fainter than any currently known, the key building blocks of $\sim L^*$ galaxies in the local universe.
2. To characterize the stellar populations of faint galaxies at high redshift and solidify our understanding of the stellar mass function at the earliest times.
3. To provide, for the first time, a statistical morphological characterization of star-forming galaxies at $z > 5$.
4. To find $z > 8$ galaxies stretched out enough by foreground clusters to measure sizes and internal structure and/or magnified enough for spectroscopic follow-up.

The Frontier Fields (FF) combines several previous high-redshift galaxy observing strategies to achieve these aims: very deep multiband *HST* imaging to identify very faint distant galaxy candidates by their color, and strong gravitational lensing by massive clusters of galaxies to probe galaxies fainter than those accessible with direct "blank" field *HST* imaging. Deep imaging with the *Spitzer* IRAC 3.6 and 4.5 μm bands is also required to improve photometric redshifts, measure stellar masses and specific star formation rates, and rule out low-redshift interlopers (e.g., Labbé et al. 2013; Bradač et al. 2014). The clusters and their exact pointings were selected to optimize the number of detectable $z \sim 10$ objects within the *HST* WFC3/IR field of view magnified by factors of ~1.5–100, depending on their positions relative to the critical curves of the clusters. The *HST* exposure times were chosen to probe intrinsic depths up to and more than 10 times fainter than the HUDF in the highest magnification regions of the lensed fields (intrinsic magnitudes ~32, with a magnification factor of 20–30), but with significantly less observing time. The volumes probed at the highest magnifications are very small (see Coe et al. 2015) with significant cosmic variance for rare and high-redshift galaxies (e.g., Robertson et al. 2015), thus the program observes multiple clusters to improve the statistical likelihood of capturing the light from the faintest and most distant galaxies. While color, redshift, and other relative measures such as specific star formation rates and emission-line equivalent widths are immune to errors in the magnification estimates, measurements of the intrinsic luminosities and sizes of individual objects depend directly on the inferred lensing magnifications. (Integrated quantities such as galaxy luminosity functions are less susceptible to magnification uncertainties.) In concert with the observing campaigns using Director's discretionary time, a unified effort to create high-fidelity public maps of the lensing properties of each FF cluster is an integral part of the FF (see Section 6).

Because each cluster is observed at a fixed *HST* roll angle for an extended period, we also obtain simultaneous deep parallel field observations at a single pointing centered ~6 arcmin from the cluster core (>1.8 projected co-moving Mpc for a $z > 0.3$ lensing cluster). These six new "blank fields" are comparable in depth to the HUDF parallel fields (Oesch et al. 2007), and triple the area of unlensed fields observed by *HST* to a depth of ~29th ABmag. The background volumes lensed by the clusters are much smaller than those probed by unlensed fields. Thus, while the cluster pointings allow us to see intrinsically fainter objects than the HUDF within small volumes, the parallel fields

provide a dramatic improvement in the volume and statistical counting of distant galaxies brighter than 29th magnitude. This is particularly important for understanding the biases associated with cosmic variance, i.e., the fact that every single sightline through the universe is unique (e.g., Robertson et al. 2014).

The Frontier Fields will set the stage for the *JWST* to study first-light galaxies at $z > 10$ and to understand the assembly of galaxies over cosmic time. *JWST* is a 6.5 m cold telescope sensitive at 0.7–27 μm, to be launched at the end of 2018 with a limited lifetime requirement of 5 yr and a goal of 10 yr. Because *JWST*'s lifetime is short relative to *HST*'s, it is important for the astronomical community to be prepared for *JWST* observations early on. The high-redshift galaxy candidates detected by the Frontier Fields are likely to be among the first spectroscopic targets for *JWST*, and current studies will produce a better understanding of the high-redshift galaxy luminosity functions, spectral energy distributions, and sizes needed to effectively plan for *JWST* surveys. The *HST* Frontier Fields (HFF) high-resolution optical imaging shortward of 0.7 μm in ACS F435W and F606W reaches depths comparable to those achieved by *JWST* NIRCam within 1–2 hr, and hence provides an important legacy data set for future *JWST* extragalactic work. Finally, direct observations of the faintest first galaxies and the dwarf galaxies and early accreting black holes expected to be responsible for reionization will be challenging even with *JWST*. Development of cluster lens modeling techniques now will enable future *JWST* studies of strong-lensing clusters and their lensed galaxies.

The Frontier Fields data offer the opportunity to do groundbreaking science in a number of fields other than the highest redshift universe. Several complementary *HST* General Observer (GO) observing programs have been awarded to obtain deep WFC3/UV imaging (GO 13389, 14209; PI B. Siana; Alavi et al. 2016), WFC3/IR grism spectroscopy (GO 13459; T. Treu), and target-of-opportunity follow-up of transient events (GO 13386, 13790, 14208; S. Rodney). Hundreds of multiply imaged background galaxies at all redshifts have permitted the construction of dark-matter maps of the clusters at unprecedented resolution to probe cluster substructure (e.g., Jauzac et al. 2014, 2015; Wang et al. 2015; Hoag et al. 2016; Limousin et al. 2016; Mohammed et al. 2016; P. Natarajan 2017 in preparation), and will enable new cosmological constraints via angular scaling relations (e.g., Kneib & Natarajan 2011). At the recommendation of the HFF review committee, an exercise comparing the various independent lens modeling methodologies and their fidelity has been on-going and results where more than 10 independent research groups participated are now in preparation (Meneghetti et al. 2016). Detailed studies of galaxies observed both at high magnification and in deep parallel imaging will probe their internal structures, stellar populations, and luminosity functions (e.g., Livermore et al. 2012; Alavi et al. 2014, Jones et al. 2015; Castellano et al. 2016a; Pope et al. 2016) These deepest-ever images of massive galaxy clusters have detected intracluster light, ram-pressure stripping, and tidal streams at $z > 0.3$ (e.g., Montes & Trujillo 2014; McPartland et al. 2016), probing the dynamic processes impacting galaxy evolution within these unique environments. The new *HST* Frontier Fields observations have detected a number of transients (e.g., Rodney et al. 2015), including the light curves from the first multiply imaged supernova (Kelly et al. 2015; discovered in GLASS).

3. Target Selection

The six Frontier Field clusters and parallel fields (Table 1) were selected to meet the primary scientific goals outlined in the HDFI SWG recommendations, as well as to optimize the *HST* and *Spitzer* observing campaigns. A list of 25 cluster candidates was suggested by the HDFI SWG, and additional candidates were suggested by the community during the selection process. Each cluster was evaluated using the following criteria.

Lensing properties. The primary consideration for selecting each of the Frontier Fields was the lensing strength of the cluster. Each cluster's lensing strength was evaluated by calculating the likelihood of observing a $z = 9.6$ galaxy magnified to $H_{F160W} \leqslant 27$ ABmag within the *HST* WFC3/IR field of view, ignoring corrections for incompleteness or sky brightness (Table 2). This metric encapsulates several constraints into a single number, making it straightforward to compare different clusters. It was calculated based on cluster lens models and a nominal blank-field luminosity function. Preliminary lens models were provided by two independent modelers, J. Richard and A. Zitrin. We adopted a luminosity function with $\phi^* = 4.27 \times 10^{-4}$, $M^*_{UV} = -19.5$, and $\alpha = -1.98$, extrapolated from $z \sim 8$ (Bradley et al. 2012) by assuming $dM^*/dz = 0.46$ (Coe et al. 2015). Actual expectations at $z = 9.6$ might be lower (e.g., Oesch et al. 2014; Bouwens et al. 2014), but the choice of luminosity function does not affect the cluster rankings.

Table 2 provides updated versions of these estimates based on the publicly available version 1 lens models (see Section 6). The expectations are similarly high for all clusters. Clusters with lower expectations were generally excluded from our selection (e.g., MACSJ0329.6-0211 and MACSJ1423.8 +2404). We note in practice that cosmic variance along each lensed line of sight is likely to be an equally important factor in detection rates of high-redshift galaxies; this cannot be known a priori for a given cluster.

Because we based our selection upon the results of the lensing model predictions, our selection was biased toward better studied clusters with existing imaging and spectroscopic data from which lensing models could be constructed. Some otherwise promising clusters (e.g., El Gordo; Menanteau et al. 2012) could not be evaluated, because insufficient lensing model constraints were available at the time of selection.

We excluded several lower-redshift $z < 0.3$ strong-lensing clusters (e.g., Abell 1689) because we could not adequately sample the critical curves of the low-redshift clusters within a single WFC3/IR $2\farcm2 \times 2\farcm0$ pointing. We note that although the critical curves of the $z = 0.545$ merging cluster MACSJ0717.5+3745s could not be covered by a single WFC3/IR pointing, the probability of observing a lensed $z \sim 9.6$ galaxy was among the highest of all cluster candidates.

Sky brightness and Galactic extinction. Observations of the very faint extragalactic universe are limited by the brightness of the sky and by foreground Galactic extinction. Zodiacal light can have a significant impact on the depths obtained by *HST* and *Spitzer* imaging within a given exposure time. This background depends upon the angular distance of the target from the Sun and the ecliptic (Figure 1). Targets observed with high zodiacal backgrounds have near-infrared sky brightnesses several magnitudes brighter than the lowest zodiacal backgrounds, resulting in images with significantly lower signal-to-noise ratio within a given exposure time. Given the highly

Table 1
The Frontier Fields Locations

Cluster	Cluster Center (J2000)		Parallel Center (J2000)		Epoch1	Epoch2	Zodiacal H_{F160W}[a]	$E_{(B-V)}$[b]
	α	δ	α	δ	*HST*	*HST*	(ABmag/□″)	
Abell 2744	00:14:21.2	−30:23:50.1	00:13:53.6	−30:22:54.3	10/2013–12/2013	5/2014–7/2014	22.2/21.9	0.012
MACSJ0416.1−2403	04:16:08.9	−24:04:28.7	04:16:33.1	−24:06:48.7	1/2014–2/2014	7/2014–9/2014	22.4/22.3	0.036
MACSJ0717.5+3745	07:17:34.0	+37:44:49.0	07:17:17.0	+37:49:47.3	9/2014–12/2014	2/2015–3/2015	21.8/22.0	0.068
MACSJ1149.5+2223	11:49:36.3	+22:23:58.1	11:49:40.5	+22:18:02.3	11/2014–1/2015	4/2015–5/2015	21.9/22.0	0.020
Abell S1063	22:48:44.4	−44:31:48.5	22:49:17.7	−44:32:43.8	10/2015–11/2015	4/2016–6/2016	22.2/20.6	0.010
Abell 370	02:39:52.9	−01:34:36.5	02:40:13.4	−01:37:32.8	12/2015–2/2016	7/2016–9/2016	21.8/21.9	0.028

Notes.
[a] Typical zodiacal background in H_{F160W} for *HST* Epoch1/Epoch2 observations; computed using *HST* exposure time calculator and median observing date.
[b] Schlafly & Finkbeiner (2011), courtesy of the NASA/IPAC Extragalactic Database.

constrained roll angles required to obtain observations of a fixed parallel field with both the WFC3 and ACS cameras, we have a limited ability to mitigate the impact of the zodiacal background by constraining the solar avoidance angle (Table 1). Therefore, strong preference was given to clusters at high ecliptic latitudes. This selection criterion excluded a number of strong-lensing clusters at low ecliptic latitudes. Additionally, clusters at high Galactic latitude with low extinction were strongly preferred (Figure 1, Table 1). MACS0717.5+3745 has relatively high Galactic extinction, with $E_{B-V} = 0.068$ (Schlegel & Finkbeiner 2011). However, this cluster was the second strongest potential lenser on our list of candidates (Table 2). Estimates of the H_{F160W} zodiacal background at the epoch of observation and Galactic extinction for each cluster are given in Table 1.

Suitability of available parallel fields. The *HST* observing strategy requires the simultaneous observation of the cluster field and a blank parallel field with WFC3/IR and ACS cameras. Ideally, these parallel fields would complement the existing deep unlensed images of the HUDF and its two parallel fields, without the complication of magnification by the clusters. However, as we discuss below, this observing requirement limits the range of available roll angles, and hence locations for the parallel fields. The potential parallel field locations were selected to avoid bright stars and extended cluster structures when possible. The weak-lensing signal for each of the parallel fields was also examined where possible (J. Merten, E. Medezinski, K. Umetsu 2012, private communication). The weak-lensing signal within the parallel fields has median magnification factors between 1.02 and 1.30 for background galaxies in the range $1 < z < 9$; see discussion of each cluster for detailed estimates.

Suitability for ground-based follow-up. Follow-up of interesting objects detected in the Frontier Fields requires access to those fields from the major ground-based facilities. ALMA in particular has the potential to spectroscopically confirm the redshift of very high-redshift ($z > 6$) galaxy candidates via the [C II] 158 μm line and other atomic emission lines (e.g., da Cunha et al. 2013). Additionally, spectroscopic redshifts of multiply imaged galaxies add strong constraints to the lensing models for the clusters. Thus, access to the telescopes on Maunakea, in addition to southern facilities like ALMA and VLT, was a major consideration. Five out of the six selected clusters are visible from ALMA, with MACS0717.5+3745 as the exception (Tables 1, 2). Five out of the six clusters are visible from Maunakea, with Abell S1063 as the exception.

Existing ancillary data. The existence of supporting data was a key consideration recommended by the HDFI SWG. Many of the candidate clusters have been studied previously by space missions, including *HST*, the *Spitzer* cryo-mission with MIPS and IRAC (including 5, 8 μm channels), *Herschel*, *XMM*, and *Chandra* (see the discussion of each cluster for details). Additionally, ground-based spectroscopic and wide-field imaging survey data were evaluated from the literature. Four of the chosen clusters were drawn from the CLASH survey (Postman et al. 2012), with supporting multi-band shallow *HST* imaging, wide-field ground-based imaging (Subaru), spectroscopy (VLT), as well as archival *Herschel* and *Chandra* data. Since the announcement of the Frontier Field selection, the community has responded with additional observations with *Chandra* (PI S. Murray, C. Jones-Forman), VLA (PI E. Murphy), *XMM* (PI J. P. Kneib, Eckert et al. 2015), ALMA (PI F. Bauer), LMT (PI A. Pope), Gemini GeMS/GSAOI K_s imaging (e.g., Schirmer et al. 2015), VLT Hawk-I K_s imaging (PI D. Marchesini & G. Brammer), VLT MUSE spectroscopy (PIs K. Caputi & Clément, F. Bauer, J. Richard, C. Grillo, e.g., Karman et al. 2015, Grillo et al. 2016), as well as the release of previously unpublished data on these fields (e.g., Ebeling et al. 2014, Gruen et al. 2014). Additional *HST* WFC3 ultraviolet imaging (Alavi et al. 2016) and grism spectroscopy (Schmidt et al. 2014) are also being obtained for all the Frontier Field clusters. We continue to maintain a clearing-house website for public data links and Frontier Fields-related publications: www.stsci.edu/hst/campaigns/frontier-fields/FF-Data.

In addition to the science-driven considerations given above, we optimized the cluster selection for a number of practical issues.

HST observability. The Frontier Fields are observed with *HST* at a fixed roll angle and its 180° offset in order to obtain deep observations in the cluster field and parallel field with both WFC3/IR and ACS. These observations consist of 70 orbits at each orientation. Each field was evaluated to determine the ability to hold a fixed roll angle for more than 30 days and the availability of guide stars at these orientations. For optimal stability, *HST* requires two guide stars brighter than 15th magnitude. Our initial evaluation of MACSJ1149.5+2223 found only one acceptable guide star; however, a second guide star with a magnitude slightly fainter than the nominal limit was available. This new guide star was tested in early observations and found to be suitable.

Spitzer observability. Each cluster and parallel field was evaluated by the *Spitzer* implementation team. *Spitzer*

Table 2
Frontier Fields: Cluster Properties and Ancillary Data

Cluster	z[a]	M_{vir}[a] ($M_\odot$)	L_X[a] (erg s^{-1})	$P(z=9.6)$[b] $H \leqslant 27$	Parallel μ[c]	*Spitzer* MIPS 24 μm	*Herschel*[d] PACS/SPIRE	ALMA[e]
Abell 2744	0.308	1.8×10^{15}	3.1×10^{45}	0.69 ± 0.07	1.14–1.21	yes	100/250/350/500	yes
MACSJ0416.1−2403	0.396	1.2×10^{15}	1.0×10^{45}	0.63 ± 0.12	1.09–1.16	no	100/250/350/500	yes
MACSJ0717.5+3745	0.545	2–3 $\times 10^{15}$	3.3×10^{45}	0.84 ± 0.05	1.07–1.42	yes	100/250/350/500	no
MACSJ1149.5+2223	0.543	2.5×10^{15}	1.8×10^{45}	0.60 ± 0.10	1.02–1.07	no	70/100/250/350/500	yes
Abell S1063	0.348	1.4×10^{15}	1.8×10^{45}	0.69 ± 0.08	1.02	yes	70/100/250/350/500	yes
Abell 370	0.375	$\sim 1 \times 10^{15}$	1.1×10^{45}	0.90 ± 0.08	1.2–1.3	yes	100/250/350/500	yes

Notes.
[a] See the text for references for each cluster.
[b] Median probability of lensing a $z = 9.6$ background galaxy to apparent H_{F160W} ABmag $\leqslant 27$ within the WFC3/IR field of view, calculated using the pre-HFF v1.0 lensing models.
[c] Median magnification factor μ in the parallel fields within the WFC3/IR field of view; based on the weak-lensing estimates from pre-HFF v1.0 Merten models. Note that magnification factors may be larger at locations closer to the cluster.
[d] See Rawle et al. (2016) for a summary of *Herschel* and *Spitzer* cryogenic observations. Note that the *Herschel* SPIRE 250/350/500 mm field of view covers both cluster and parallel fields for all but MACSJ0416.1-2403.
[e] Visibility from ALMA.

observations are sensitive to bright stars in the field, because saturation above ∼35,000 DN can result in "column pull-down" impacting the data quality along the affected column. MACSJ0647.7+7015 (e.g., Coe et al. 2013) in particular was found to have unacceptably bright stars in the vicinity, and was excluded.

Scheduling. Each set of cluster/parallel field observations constitutes a considerable investment of *HST* time, with 70 orbits at each orientation and 140 orbits total per field. The optimal scheduling of these observations is a challenge. We also anticipated that the Frontier Fields would be popular fields for ancillary *HST* observing programs. Therefore to avoid schedule collisions with the main Frontier Field program, supporting Frontier Field programs, and other popular *HST* fields (e.g., the UDF/GOODS-S), the Frontier Fields were selected to span a range in R.A. The order in which the fields are observed was determined primarily by the desire to prevent overlapping epochs of *HST* observations.

JWST observability. Each of the selected Frontier Fields positions was run through preliminary *JWST* scheduling software and confirmed to have extended periods of *JWST* visibility.

4. The Frontier Field Clusters and Parallel Fields

In 2013 February, the six Frontier Field clusters and their parallel field locations were finalized and announced prior to the *HST* Cycle 21 proposal deadline. The Frontier Field clusters are Abell 2744, MACSJ0416.1-2403, MACSJ0717.5+3745, MACSJ1149.5+2223, Abell S1063 (also known as RXCJ2248.7-4431), and Abell 370 (Table 1). These clusters are at redshifts between 0.3 and 0.55, and are among the most massive known clusters at these redshifts (Table 2). All of the clusters had previous (shallow) *HST* imaging, with four clusters previously observed as part of the CLASH *HST* MCT survey (MACSJ0416.1-2403, MACSJ0717.5+3745, MACSJ1149.5+2223, and Abell S1063) and all but Abell 370 were part of the Massive Clusters Survey (Ebeling et al. 2001).

4.1. Abell 2744

Abell 2744 (Figure 2) is a massive X-ray-luminous merging cluster at $z = 0.308$, (Couch & Newell 1982; Abell et al. 1989), also known as AC118 or "Pandora's Cluster." It has a total X-ray luminosity of $L_X = 3.1 \times 10^{45}$ erg s^{-1} at 2–10 keV (Allen 1998), with X-ray emission concentrated on the southern compact core and extending to the northwest (Owers et al. 2011; Eckert et al. 2015). Its virial mass within the central 1.3 Mpc is $\sim 1.8 \times 10^{15}\, M_\odot$ (Merten et al. 2011). The velocity dispersion is $\sigma = 1497 \pm 47$ km s^{-1} (Owers et al. 2011), but shows two distinct structures, with the northern substructure offset in velocity by -1600 km s^{-1} and $\sigma \sim 800$ km s^{-1} (Boschin et al. 2006; Braglia et al. 2007). Abell 2744's complicated velocity structure and lensing properties suggest that it is a merging system with at least three separate substructures (Cypriano et al. 2004; Braglia et al. 2007; Merten et al. 2011). Weak-lensing analysis by Merten et al. (2011) identified four mass concentrations labeled core, N, NW, W of 2.2, 0.8, 1.1, $1.1 \times 10^{14}\, M_\odot$ respectively, with the NW structure showing evidence for spatially separated dark matter, gas, and galaxies. Abell 2744 is also host to a powerful extended radio halo with $P_{1.4\,\mathrm{GHz}} = 1.5 \times 10^{25}$ W Hz^{-1} (Giovannini et al. 1999).

Despite its obviously complicated geometry, Abell 2744 was one of the strongest Frontier Field cluster candidates based on its lensing strength, sky location, and pre-existing ancillary data. The pre-FF lensing model by Merten et al. (2011; using the Light-traces-mass modeling method of Zitrin et al. 2009a) found 34 strong-lensed images of 11 galaxies in *HST* F814W imaging of the core of Abell 2744 (*HST* GO 11689, PI R. Dupke), giving a core mass $\sim 2 \times 10^{14}\, M_\odot$. This core region is $\sim 100'' \times 100''$, and therefore fits within the *HST* WFC3/IR field of view of $2\farcm2 \times 2\farcm1$. Analysis of preliminary models constructed by Zitrin and Richard separately suggested a very high probability of magnifying a $z \sim 10$ galaxy to $H = 27$ ABmag within the WFC3/IR field of view. This high lensing probability has been confirmed by subsequent models provided by the lensing map effort and independent teams (e.g., Atek et al. 2014; Johnson et al. 2014; Lam et al. 2014; Richard et al. 2014; Zitrin et al. 2014; Coe et al. 2015; Ishigaki et al. 2015; Jauzac et al. 2015; Wang et al. 2015; Table 2).

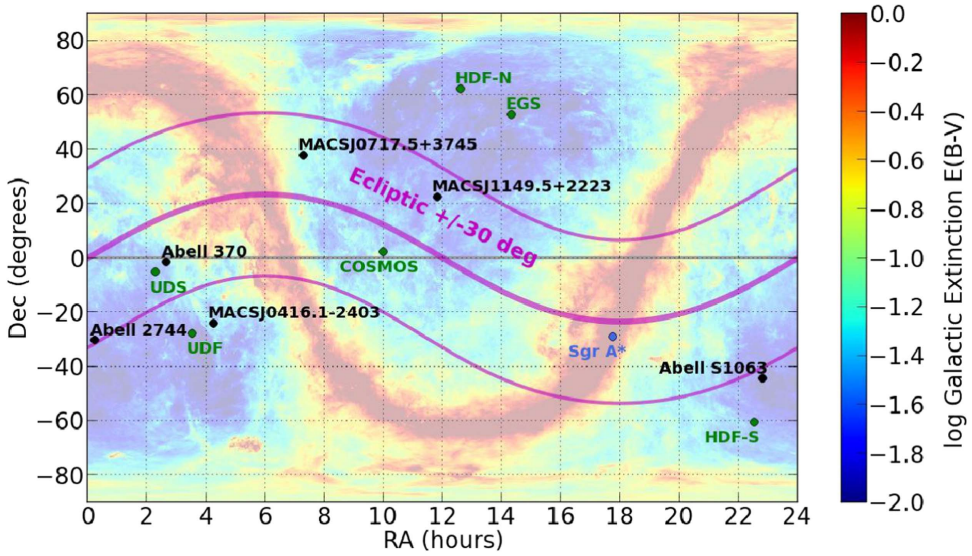

Figure 1. Location of the six Frontier Field cluster + parallel field pairs, relative to the ecliptic and Galactic plane. The Galactic extinction map is from Schlegel et al. (1998). Deep extragalactic legacy fields HDF-N, HDF-S, UDF, COSMOS, EGS, and UDS are shown for reference.

Abell 2744 has one of the darkest skies and lowest Galactic extinctions, $E_{(B-V)} = 0.012$ (Schlafly & Finkbeiner 2011), of all the cluster candidates. The typical zodiacal background in H_{F160W} during the cluster IR epoch (10/2013–12/2013) and the parallel IR epoch (5/2014–7/2014) is ∼22.2 and 21.9 ABmag per □″ respectively. At a decl. of −30, it is easily observable with ALMA and the VLT but also within reach of Maunakea and the Very Large Array. It has been extensively studied by the *Chandra X-ray Observatory* (e.g., Kempner & David 2004; Merten et al. 2011; Owers et al. 2011). Abell 2744 was also observed during the *Spitzer* cryo-mission, with MIPS 24 μm and IRAC 3.6–8 μm observations (PI G. Rieke). This cluster is part of the *Herschel* Lensing Survey (Egami et al. 2010), with deep *Herschel Space Observatory* PACS 100/160 μm and SPIRE 250/350/500 μm imaging.

The choice of parallel field (Figure 3, Table 1) was particularly challenging in this case. *HST* roll angles with >30 day observing windows at both orientations placed the observable parallel field 6′ either east or west of the core of Abell 2744. However, the eastern parallel field location was undesirable because of the presence of an unavoidable bright star. Therefore the western parallel field location (α = 00:13:53.6, δ = −30:22:54.3, J2000) was chosen. The parallel field is ∼1′–2′ west of the NW and W substructures identified in Merten et al. (2011). The weak-lensing magnification boost from the cluster is therefore predicted to be significant, with median magnification factors ∼1.14–1.21 and maximum magnification factors 1.5–1.85 for $1 < z < 9$ within the WFC3/IR pointing based on the pre-HFF v1.0 Merten model (Table 2).

4.2. MACSJ0416.1-2403

MACSJ0416.1-2403 (Figure 4(a)) is a massive elongated X-ray-luminous cluster at $z = 0.397$ (Ebeling et al. 2007, 2014).[12] Its bolometric X-ray luminosity is $L_x = 1.02 \times 10^{45}$ erg s^{-1}, with a double-peaked profile suggestive of a merging cluster (Mann & Ebeling 2012). The velocity dispersions for each of these components are $\sigma = 779^{+22}_{-20}$ and 955^{+17}_{-22} km s^{-1} (Ebeling et al. 2014; Jauzac et al. 2014), and the total mass enclosed within 950 kpc ∼1.2×10^{15} $M_\odot$ (Jauzac et al. 2014; Grillo et al. 2015). MACSJ0416.1-2403 was selected as one of five strong-lensing clusters for the CLASH *HST* MCT survey (Postman et al. 2012) based on its large Einstein radius ($\theta_E > 0\farcs35$ at $z = 2$). Prior to the Frontier Fields observations, Zitrin et al. (2013) found a high number of multiple images relative to its critical area in the CLASH *HST* images, likely due to its highly elongated and irregular structure.

Preliminary evaluation of MACSJ0416.1-2403's lensing models yielded moderate to high probabilities of detecting a $z \sim 10$ $H \leqslant 27$ mag galaxy within the WFC3/IR field of view (Table 2). MACSJ0416.1-2403 is at a high ecliptic latitude with a Galactic extinction $E(B-V) = 0.036$ (Schlafly & Finkbeiner 2011). The typical zodiacal background in H_{F160W} during the cluster IR epoch (7/2014–9/2014) and the parallel IR epoch (1/2014–2/2014) is ∼22.3 and 22.4 ABmag per □″ respectively. At decl. ∼ −24, this field is easily observable with ALMA, and also available to Maunakea. A significant amount of data was collected on this cluster as part of MACS and CLASH, including shallow multi-band *HST* data, *Chandra* imaging, *Spitzer* warm-mission IRAC (PI R. Bouwens), and VLT spectroscopy (e.g., Grillo et al. 2015). Additional *Chandra* imaging has since been obtained by C. Jones-Forman and S. Murray (Ogrean et al. 2015). However, there are no legacy *Spitzer* cryogenic observations.

MACSJ0416.1-2403 is notable for having a $J = 10$, $V = 13$ magnitude star within 1′ of the cluster core. This star has a high proper motion, with DSS and 2MASS imaging from the mid-1990s showing a position a few arcseconds north of its current (2014) *HST* ACS position. This star is included in the Frontier Fields ACS pointing and lies just off the WFC3/IR pointing, resulting in scattered light and saturated diffraction spikes in the Frontier Field images. However, this star is bright enough to act as a guide star for adaptive optics, and therefore provides a unique opportunity to obtain adaptive optics imaging (e.g., Schrimer et al. 2015; Gemini-GEMS) and spectroscopy of the critical curves surrounding a strong-lensing cluster.

[12] This cluster's redshift is often incorrectly quoted as 0.42, based on preliminary analysis by Postman et al. (2012).

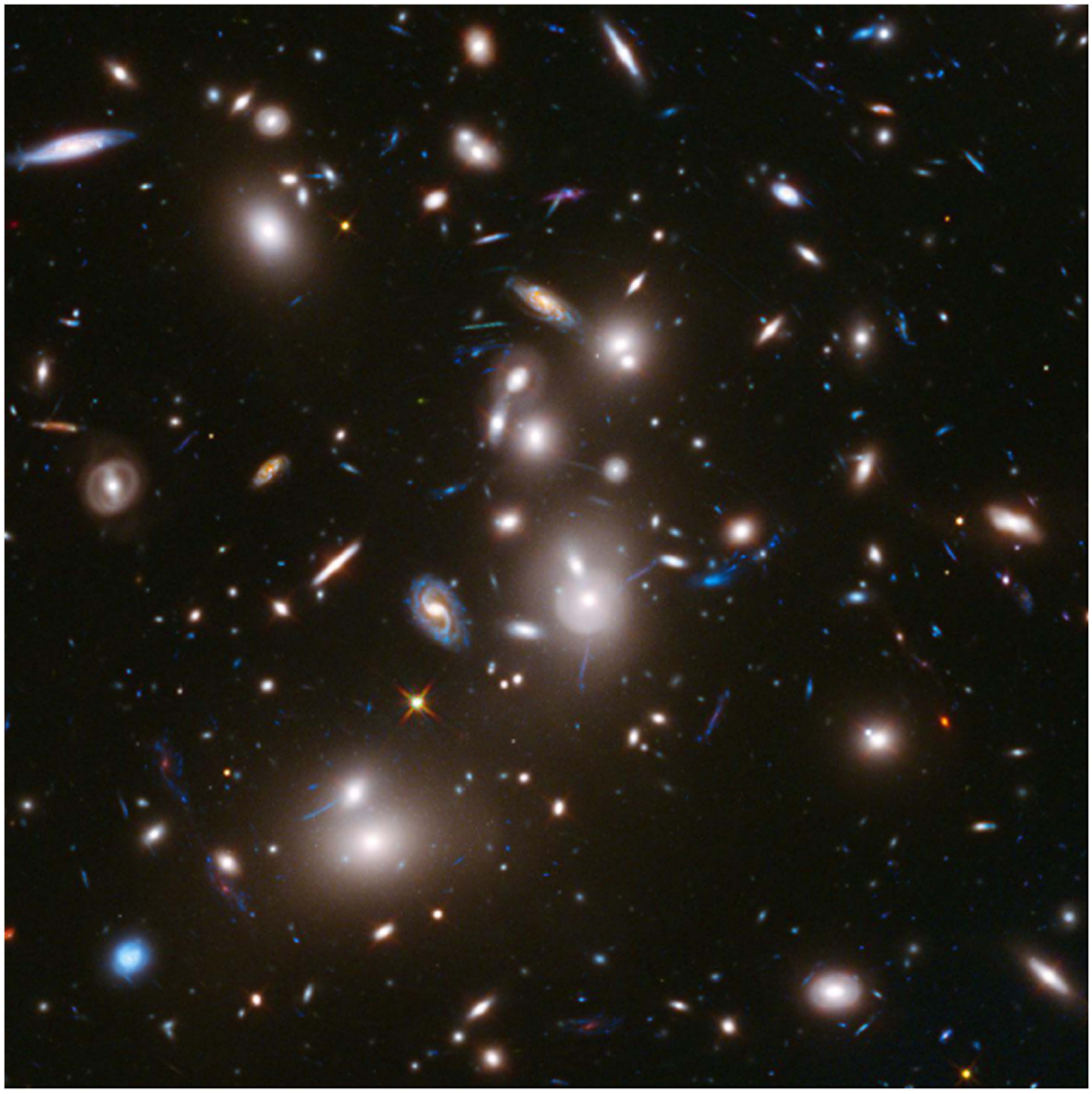

Figure 2. *HST* full-depth image of Abell 2744, the first Frontier Field strong-lensing cluster. The central $1\farcm5 \times 1\farcm5$ is shown.

The MACSJ0416.1-2403 parallel field (Figure 4(b), Table 1) was chosen to lie westward of the cluster pointing in order to avoid the bright eastern stars in the *Spitzer* Frontier Field observations. This orientation is perpendicular to the elongation of the cluster on the sky, and therefore we expect minimal contamination of the parallel field from the cluster. The parallel field is predicted to have median magnification factors ∼1.09–1.16 and maximum magnification factors 1.2–1.4 for $1 < z < 9$ within the WFC3/IR pointing based on the pre-HFF v1.0 Merten model (Table 2).

4.3. MACS0717.5+3745

MACSJ0717.5+3745 (Figure 5(a)) is an extremely massive X-ray-luminous merging cluster at $z = 0.545$ (Edge et al. 2003). The X-ray luminosity between 0.1 and 2.4 keV is $(3.3 \pm 0.2) \times 10^{45}$ erg s^{-1} (Edge et al. 2003). The cluster's velocity dispersion is 1660^{+120}_{-130} km s^{-1} (Ebeling et al. 2007). Its optical and X-ray morphology shows a double peak and a lack of center cluster core, with a filament extending southeast (Ebeling et al. 2004; Kartaltepe et al. 2008). This cluster also hosts the most powerful known radio source ($P_{1.4\,\mathrm{GHz}} \sim 5 \times 10^{25}$ W Hz^{-1}) with a radio relic significantly offset from the cluster center to the north (van Weeren et al. 2009). MACSJ0717.5+3745 was also chosen as one of the CLASH strong-lensing clusters (Postman et al. 2012). It has the largest known Einstein radius (∼350 kpc, Zitrin et al. 2009b) and an estimated virial mass $\geq$2–3 $\times 10^{15}\,M_{\odot}$ (Zitrin et al. 2009b; Limousin et al. 2012). Several pointings of *HST* ACS imaging were obtained previously by Ebeling in Cycle 12 (GO 9722). Weak-lensing analyses of the pre-Frontier Fields *HST* imaging and ground-based Subaru imaging have confirmed the presence of the southeast filament, with a projected length of ∼4.5 Mpc and true length of ∼18 Mpc (Jauzac et al. 2012; Medenski et al. 2013).

Independent preliminary lensing models from Zitrin and Richard ranked MACS0717.5+3745 as the strongest lenser of all the clusters considered (see Table 2). However, MACSJ0717.5+3745 has the highest zodiacal background of all the Frontier Fields, as well as a relatively high Galactic extinction $E_{(B-V)} = 0.068$ (Schlafly & Finkbeiner 2011). It has

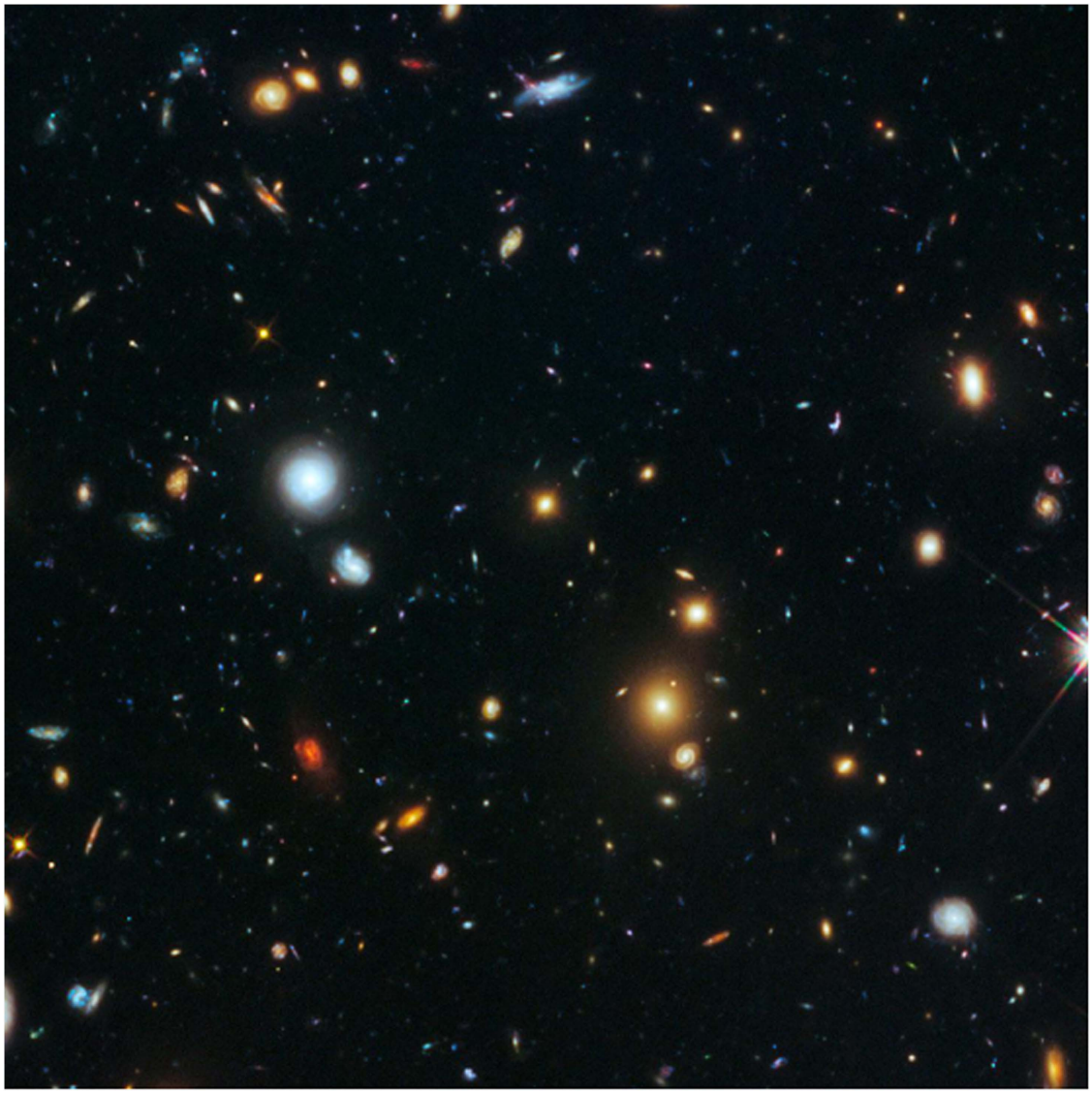

Figure 3. *HST* full-depth image of the Abell 2744 parallel field (central $1\farcm5 \times 1\farcm5$).

an ecliptic latitude of 15°.4, with a typical zodiacal background in H_{F160W} during the cluster IR epoch (2/2015–3/2015) and the parallel IR epoch (9/2014–12/2014) of ∼22.0 and 21.8 ABmag per □″ respectively. It is also our northernmost cluster at decl. >30°, placing it just out of reach of ALMA and other southern observatories. As a CLASH cluster, significant shallow *HST* imaging, ancillary wide-field Subaru imaging, and a photometric redshift catalog are available. This cluster was also observed with the *Spitzer* cryogenic mission with both IRAC and MIPS (PI D. Kocevski) and the *Spitzer* warm-mission SURFSUP program (PI M. Bradač; Bradač et al. 2014), as well as with the *Herschel Space Observatory* (Egami et al. 2010). A spectroscopic redshift catalog was recently published by Ebeling et al. (2014).

The MACSJ0717.5+3745 parallel field (Figure 5(b)) was chosen to lie northwest of the cluster pointing in order to avoid the long cluster filament extending to the southeast. The parallel field is predicted to have median magnification factors ∼1.07–1.15 and maximum magnification factors 1.17–1.42 for $1 < z < 9$ within the WFC3/IR pointing based on the pre-HFF v1.0 Merten model (Table 2).

4.4. MACS1149.5+2223

MACSJ1149.5+2223 (Figure 6(a)) at $z = 0.543$ was discovered as part of the MACS survey as one of the most X-ray-luminous clusters known at $z > 0.5$ (Ebeling et al. 2001, 2007). Its 0.1–24 keV X-ray luminosity is $L_x = (1.76 \pm 0.04) \times 10^{45}$ erg s^{-1} and it has a velocity dispersion of 1840^{+120}_{-170} km s^{-1} (Ebeling et al. 2007). Its optically selected galaxy population and X-ray morphology are elongated within the cluster core, but do not show evidence of extended filaments (Kartaltepe et al. 2008). Spectroscopic studies and lensing analysis of previous *HST* ACS imaging (PI H. Ebeling; GO 9722) suggest four or more large-scale dark-matter subhaloes and a complex merger history (Zitrin & Broadhurst 2009; see also Smith et al. 2009). A CLASH strong-lensing cluster (Postman et al. 2012), it has a large Einstein radius (∼170 kpc, Zitrin & Broadhurst 2009) and an estimated total mass $\sim 2.5 \times 10^{15}\, M_\odot$ (Zheng et al. 2012). Based on the CLASH imaging, Zheng et al. (2012) reported a singly imaged $z = 9.6$ galaxy candidate with a magnification ∼14.5 and observed F160W magnitude ∼26.5.

Preliminary lensing models from Zitrin and Richard ranked MACSJ1149.5+2223 as a moderate lenser (Table 2). Its

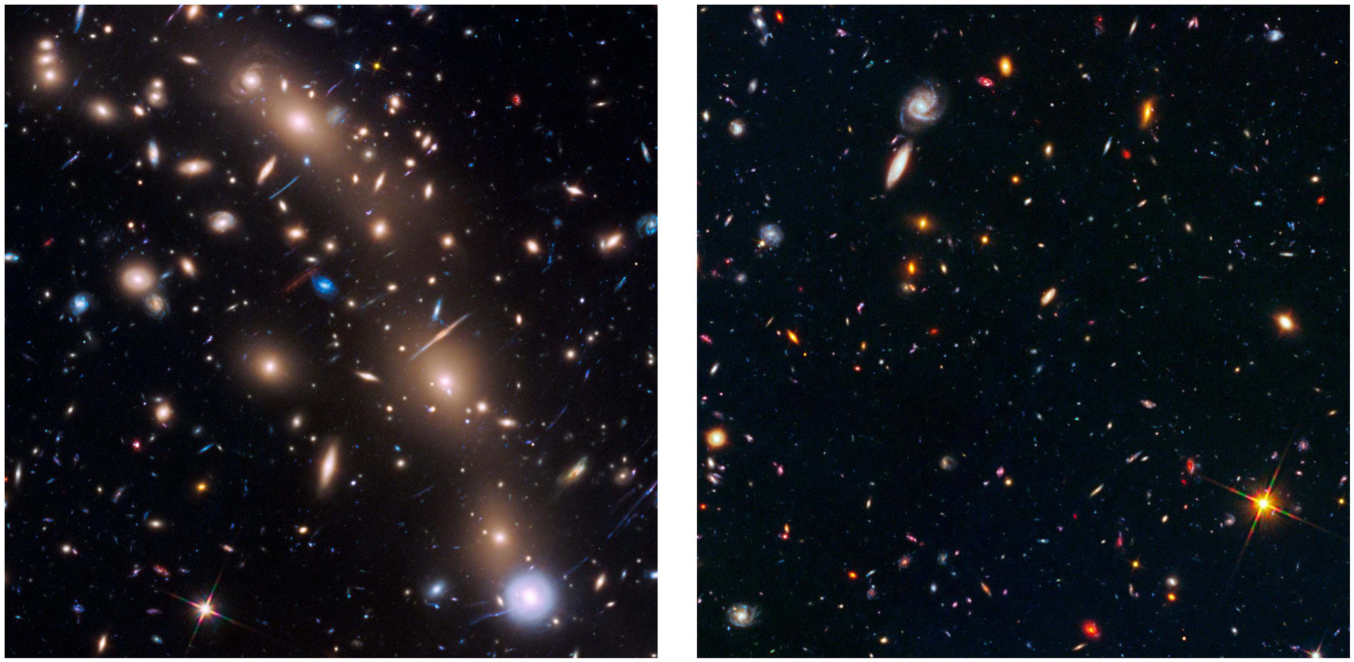

Figure 4. *HST* full-depth image of MACSJ0416.1-2403 and its parallel field (central $1\farcm5 \times 1\farcm5$).

Galactic extinction is fairly low, $E(B-V) = 0.020$ (Schlafly & Finkbeiner 2011), and it has a zodiacal background $\sim 22 H_{F160W}$ ABmag per $\square''$ during the epochs of observation (cluster IR: 11/2014–1/2015; parallel IR: 4/2015–5/2015). Initially, this cluster was not considered an ideal *HST* target because only one bright guide star was known at the required orientation. However, further investigation revealed a second guide star slightly fainter than the nominal magnitude cutoff, and early observations of MACSJ1149.5+2223 in Cycle 21 confirmed the suitability of this guide star pair. At decl. $+22°$, this cluster is barely observable with ALMA but easily observed from Maunakea and other northern observatories like the Very Large Array. This cluster is part of the Herschel Lensing Survey (Egami et al. 2010) and a GT Cycle 1 program (PI D. Lutz), and was targeted by the *Spitzer* warm-mission SURFSUP IRAC imaging program (Bradač et al. 2014).

The southern position for the MACSJ1149.5+2223 parallel field (Figure 6(b), Table 1) was chosen to avoid a particularly bright star at the northern position. The parallel field is predicted to have median magnification factors ∼1.02–1.07 and maximum magnification factors 1.1–1.3 for $1 < z < 9$ within the WFC3/IR pointing based on the pre-HFF v1.0 Merten lensing model (Table 2).

4.5. Abell S1063

Abell S1063 (also known as RXC J2248.7-4431 and SPT-CL J2248-4431), is the southernmost Frontier Fields cluster with $z = 0.3461$ (Abell et al. 1989; Böhringer et al. 2004; Gómez et al. 2012). Abell S1063 is a massive cluster with a large velocity dispersion 1840^{+230}_{-150} km s^{-1}. Its X-ray luminosity between 0.5 and 2.0 keV is $(1.8 \pm 0.2) \times 10^{45}$ erg s^{-1} (Williamson et al. 2011), and the cluster has one of the highest known X-ray temperatures (>11.5 keV) (Gómez et al. 2012). It is also among the clusters most strongly detected via the Sunyaev–Zel'dovich (SZ) effect in the South Pole Telescope survey (Williamson et al. 2011), with an SZ-derived mass $M_{500} \sim 1.4 \times 10^{15} M_{\odot}$. Like the other Frontier Field clusters, its map of galaxy density shows significant substructure, with an X-ray peak offset from the primary peak of galaxy density (Gómez et al. 2012). Weak-lensing analysis also identified multiple substructures, and gives a mass of the central cluster in agreement with X-ray and SZ calculations (Gruen et al. 2013). Selected as a CLASH cluster, the *HST* imaging revealed a quintuply lensed $z \sim 6$ galaxy (Balestra et al. 2013; Monna et al. 2013). The images from the Herschel Lensing Survey (Egami et al. 2010) show an associated 870 μm source, a lensed submillimeter galaxy with one of the highest redshifts known (Boone et al. 2013).

Abell S1063 is one of the less powerful lensers (Table 2) and the most relaxed of the selected Frontier Fields clusters. However, it is located in one of the darkest regions of the sky, with a Galactic extinction of $E_{(B-V)} = 0.010$ (Schlafly & Finkbeiner 2011). The typical zodiacal background is 20.6 and 22.2 H_{F160W} ABmag per $\square''$ during the cluster IR epoch (4/2016–6/2016) and the parallel IR epoch (10/2015–11/2015) respectively. It is inaccessible from Maunakea but easily observed by ALMA and the VLT. As an SPT (South Pole Telescope) and CLASH cluster, it had extensive spectroscopic and ancillary data already, including shallow *Chandra* imaging (PI A. Romer), *Herschel* (Egami et al. 2010; also Open Time Cycle 2 program, PI T. Rawle), SZ, *Spitzer* cryo-mission MIPS and IRAC (PI G. Rieke), and VLT spectroscopy (e.g., Balestra et al. 2013). Recently, Abell S1063 has been targeted by the VLT MUSE integral field spectrograph (Karman et al. 2015).

The Abell S1063 parallel field was chosen to the east of the cluster, to avoid scattered light from the western bright stars in the *Spitzer* and *HST* observations. We note that Gruen et al. (2013) report an east–northeast cluster substructure that lies northward of the location of the Abell S1063 parallel field. The parallel field is predicted to have median magnification factors ∼1.02 and maximum magnification factors of 1.27–1.43 for $1 < z < 9$ within the WFC3/IR pointing based on the pre-HFF v1.0 Merten lensing model.

Figure 5. *HST* full-depth image of MACSJ0717.5+3745 and its parallel field (central $1\farcm5 \times 1\farcm5$).

4.6. Abell 370

Abell 370 (Abell 1958) at $z = 0.375$ (Struble & Rood 1999) is the host of the first known gravitational Einstein ring (Paczynski 1987; Soucail et al. 1987) and thus one of the best studied strong-lensing clusters (e.g., Kneib et al. 1993; Smail et al. 1996; Bezecourt et al. 1999a, 1999b; Broadhurst et al. 2008; Medezinski et al. 2010; Richard et al. 2010; Umetsu et al. 2011). Its total velocity dispersion is $\sim$1170 km s^{-1} (Dressler et al. 1999), with the two main substructures showing internal velocity dispersions of $\sim$850 km s^{-1} (Kneib et al. 1993). Abell 370's total bolometric X-ray luminosity is $L_x = 1.1 \times 10^{45}$ erg s^{-1} (Morandi et al. 2007). X-ray, SZ, and lensing analyses of Abell 370 consistently yield a virial mass $\sim 1 \times 10^{15}\ M_\odot$ (e.g., Morandi et al. 2007; Richard et al. 2010; Umetsu et al. 2011). With *HST* ACS images taken shortly after the last *HST* refurbishment, Richard et al. (2010) found significant offsets between the peak X-ray emission and peaks of the lensing mass distribution, and concluded that Abell 370 is likely the recent merger of two equal-mass clusters along the line of sight. Like Abell 2744, Abell 370 was not part of the CLASH *HST* MCT survey (Postman et al. 2012).

Abell 370 is one of the stronger lensers among the selected Frontier Fields clusters, with current models predicting $P(z = 9.6) \sim 0.9$ (Table 2). The typical zodiacal background is 21.9 and 21.8 H_{F160W} ABmag per $\square''$ during the cluster IR epoch (7/2016–9/2016) and the parallel IR epoch (12/2015–2/2016) respectively. It has a Galactic foreground extinction $E_{(B-V)} = 0.028$, and is accessible with telescopes in both the Northern and Southern Hemispheres. Abell 370 also has a rich legacy of archival data, including *Chandra* imaging (PI G. Garmire), *Herschel* data from the PACS Evolutionary Probe (Lutz et al. 2011) and *Herschel* Multi-tiered Extragalactic Survey (Oliver et al. 2012), and cryogenic *Spitzer* data in the four IRAC channels, IRS, and MIPS (PIs G. Fazio; G. Rieke; J. Houck; D. Lutz; C. Dowell).

For Abell 370, we choose the southeastern parallel position in order to avoid multiple bright stars northwest of the cluster and a possible extension of cluster members to the north (Broadhurst et al. 2008). The parallel field is predicted to have the strongest weak-lensing boost, with median magnification factors $\sim$1.2–1.32 and maximum magnification factors 1.35–1.63 for $1 < z < 9$ within the WFC3/IR pointing based on the pre-HFF v1.0 Merten lensing model.

4.7. Other Cluster Candidates

We considered a number of potential Frontier Field clusters, many of which are known to be exceptional lensers. We excluded Abell 1689, Abell 1703, Abell 2218, and the Bullet Cluster because of their low redshifts/large angular sizes of their critical curves relative to the WFC3/IR field of view. Abell 2537, MACSJ1206.2-0747, MACSJ2129.4-0741, MACSJ2214.9-1359, RCS2-2327.4-04, and RXJ1347.5-1144 all have low ecliptic latitudes, and therefore have unacceptably high zodiacal backgrounds. MACSJ0329.6-0211, MACSJ451.0+0006, MACSJ0520.7-1328, MACSJ0744.9+3927, and Cl0024.0+1652 have high Galactic extinctions ($E(B-V) > 0.05$). MACSJ0647.7+7015 and MACSJ744.9+3927 have numerous unavoidable bright stars in the field. Abell 2218, MACSJ0647.7+7015, MACSJ744.9+3927, and MACSJ1423.8+2404 are unsuitable for deep ALMA observations. MACSJ0358.8-2995 has a foreground $z = 0.17$ Abell cluster and very limited *HST* visibility. MACSJ0454.1-0300 is a weaker lenser with a moderate zodiacal background. MACSJ0257-2325 had limited public ancillary data at the time of selection. Additionally, these last three clusters are close in R.A. to each other and to the UDF/GOODS-South field and MACSJ0416.1-2403, and therefore would have posed scheduling issues for *HST* over the course of the next several *HST* cycles.

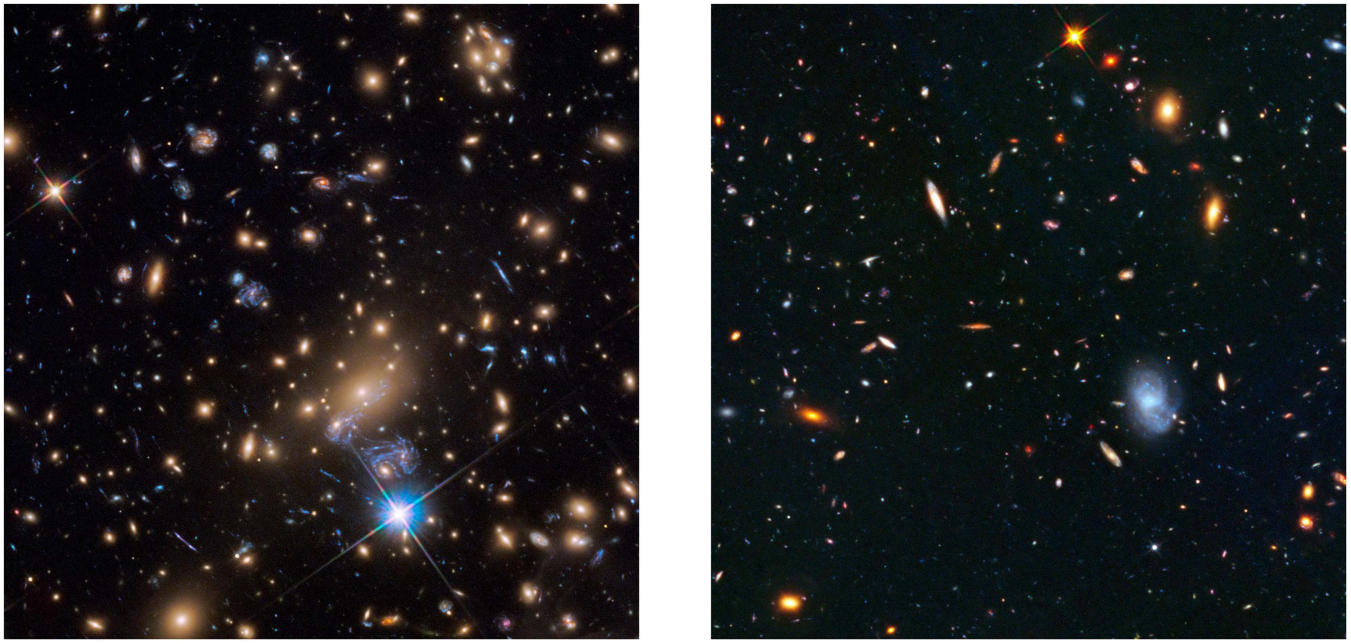

Figure 6. *HST* full-depth image of MACSJ1149.5+2223 and its parallel field (central $1\farcm5 \times 1\farcm5$).

5. Observations

Deep optical and near-infrared imaging achieving 5σ depths of ∼29th AB magnitude in seven *HST* bandpasses (ACS/WFC B_{F435W}, V_{F606W}, I_{F814W}, WFC3/IR Y_{F105W}, J_{F125W}, JH_{F140W}, H_{F160W}) from 0.4–1.6 μm is used to identify high-redshift galaxies ($z > 4$) using the Lyman break drop-out technique (Table 3, Figures 2–6). Deep *Spitzer* IRAC imaging at 3.6 and 4.5 μm places additional constraints on galaxy redshifts (Table 3, Figure 7). Fitting of the spectral energy distribution of the multi-wavelength photometry from the combined *HST* and *Spitzer* imaging (e.g., Castellano et al. 2016; Merlin et al. 2016) provides photometric redshifts and estimates of the galaxies' stellar masses and recent star formation histories (e.g., Castellano et al. 2016).

The Frontier Field cluster observations have the same exposure times as the parallel fields, and similar observed depths. However, the intrinsic depths for background galaxies lensed by the clusters are deeper than the parallel fields (considering the contribution to the foreground by the intracluster light and galaxies in the cluster; see Livermore et al. (2017) and Merlin et al. (2016) for strategies for subtracting the intracluster light), with typical magnifications across the cluster pointings of ∼1.5–2 and small areas magnified by factors as large as 10–100.

5.1. HST Observing Strategy

Both the Wide Field Camera 3 and Advanced Camera for Surveys are used in concert at fixed *HST* roll angles to probe each Frontier Field cluster and a parallel "blank" field pair. Based upon the recommended depths and filter sets from the HDFI SWG report, we obtain 70 orbits per camera at a given roll angle, for a total of 140 orbits per pointing for both the cluster and parallel field. The first four sets of Frontier Fields were awarded Director's discretionary time in Cycles 21 and 22 for a total of 560 orbits. Two more Frontier Fields were approved for *Spitzer* observations using Director's discretionary time in *Spitzer* Cycle 11 and were awarded an additional 280 orbits of Director's discretionary time in *HST* Cycle 23 after an external mid-term review of the program.[13]

Table 3
Frontier Fields Target Depths

Camera/Filter	Exposure Time[a]	5σ[b]
HST ACS/WFC F435W	45 ks	28.8
HST ACS/WFC F606W	25 ks	28.8
HST ACS/WFC F814W	105 ks	29.1
HST WFC3/IR F105W	60 ks	28.9
HST WFC3/IR F125W	30 ks	28.6
HST WFC3/IR F140W	25 ks	28.6
HST WFC3/IR F160W	60 ks	28.7
Spitzer IRAC 3.6 μm	180 ks	26.5
Spitzer IRAC 4.5 μm	180 ks	26.0

Notes.
[a] Assuming 2500 s per *HST* orbit. *Spitzer* depths include previous archival observations.
[b] Calculated for a point source within a $0\farcs4$ diameter aperture for *HST*.

Filter selection and depths: The ACS/WFC observations are taken in the B_{F435W}, V_{F606W}, and I_{F814W} filters, and the WFC3/IR observations are obtained in Y_{F105W}, J_{F125W}, JH_{F140W}, and H_{F160W} for both the parallel and cluster fields. The HDFI SWG recommended the JH_{F140W} filter for the cluster pointings only. This filter is most needed for discriminating between $z \sim 9$ and higher redshift candidates (e.g., Ellis et al. 2013), and it was felt that these would be unlikely to be detected in the parallel fields. However, subsequent input from the community and the discovery of bright $z \geqslant 9$ candidates (e.g., Oesch et al. 2014) resulted in the addition of the JH_{F140W} to the parallel field observations. The number of orbits per filter/camera and estimated depths for a 5σ point source measured within a $0\farcs4$ diameter aperture are given in Table 3. For comparison, the CLASH 5σ point-source depths are ∼26.3–27.0 AB

[13] www.stsci.edu/hst/campaigns/frontier-fields/documents/FF_MidTermReview.pdf

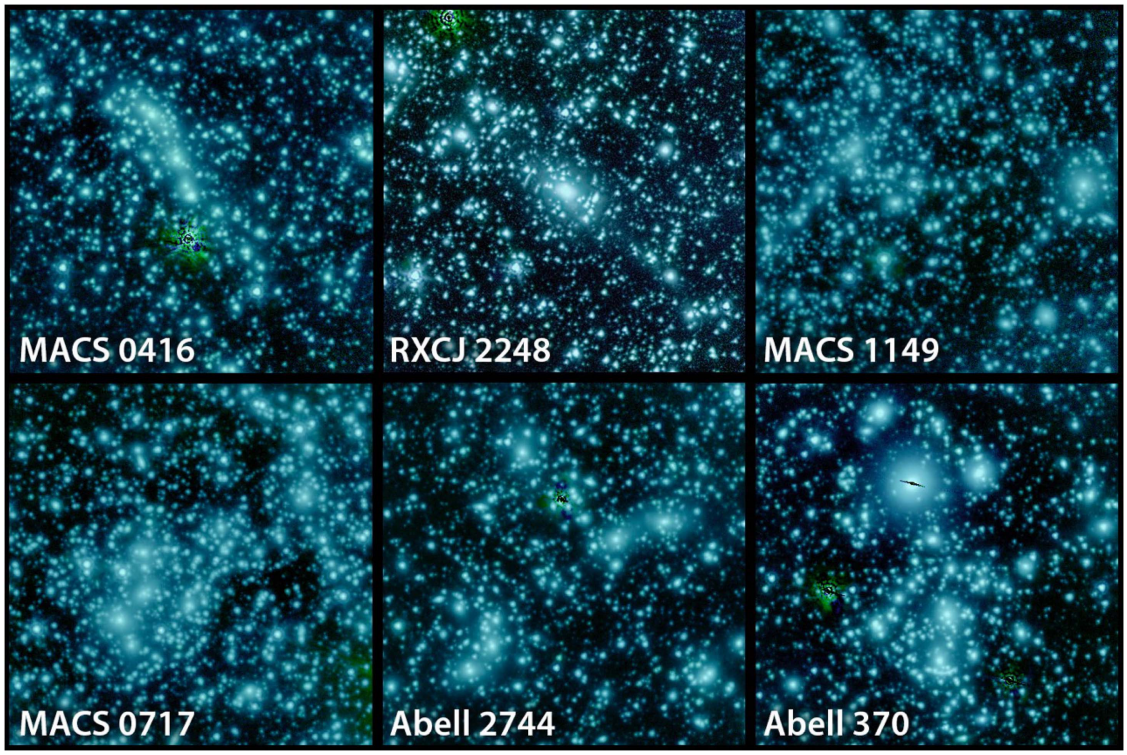

Figure 7. *Spitzer* 3.6 and 4.5 μm color images of the Frontier Fields. The field of view for each frame is $4\farcm8 \times 4\farcm8$.

magnitudes in 1–2 *HST* orbits in the same ACS and WFC3 filter sets (Postman et al. 2012).

Observational cadence. Given the large number of orbits required for a given field and orientation, we selected clusters for which *HST* observing windows were available of at least 30 days at both fixed orientations with suitable guide stars at each. The HDFI SWG did not recommend optimizing the cadence of the observations of a given field in order to search for supernovae or other transient objects (as had been done for the GOODS, CANDELS, and CLASH programs), because this would prevent holding *HST* at a fixed roll angle and obtaining deep parallel field observations. Therefore, the data for each field were obtained in two epochs of ~30–60 days (one for each camera/orientation) separated by six months. However, for those fields for which no pre-existing *HST* data were available, we obtained one advance visit with ACS/I_{F814W} and/or one advance visit with WFC3/H_{F160W} to provide a template for transients and preliminary catalogs for ground-based and *Spitzer* ancillary observations.

During each main epoch of observations, the *HST* WFC3/IR filter complement was initially rotated through $Y_{F105W}/J_{F125W}/JH_{F140W}/H_{F160W}$ with a single filter per two-orbit visit. This facilitated the detection of high-redshift supernovae despite the non-optimal cadence for SN detection. Our first set of observations of Abell 2744 were impacted by time-variable background in the WFC3/IR Y_{F105W}. This is due to a known He I emission line at 10830 Å from the Earth's atmosphere, which is detected by *HST* when it observes at low limb angles at the start or end of an orbit and *HST* is not in Earth's shadow. During the course of our observations, it was determined that we could predict the times of highly variable sky based upon the observational ephemeris (Brammer et al. 2014). Therefore, a subset of our visits for MACSJ0416.1-2403 were changed to four-orbit visits, with four half-orbit Y_{F105W} exposures paired with four half-orbit H_{F160W} exposures taken at the start (or end) of each orbit when He I emission was expected to have the largest impact. We found this strategy to work well for mitigating the impact of time-variable sky on the Y_{F105W}; remaining signatures of this effect, as well as time variability in all IR filters when observing close to the bright Earth limb, are removed from our reduced data using a modified IR ramp-fitting algorithm (Hilbert 2014; Robberto 2014).

Initially, the ACS/WFC filter complement was rotated through $B_{F435W}/V_{F606W}/I_{F814W}$ throughout each observing epoch as well. At low sky backgrounds, ACS/WFC images are degraded by charge transfer efficiency (CTE) trails. While CTE trails from sources and hot pixels are now corrected in the standard pipeline, this correction is never perfect and results in residual noise above the exposure time calculator estimates. However, in reducing the observations for the first epoch of Abell 2744, we found that the final combined images were greatly enhanced when "self-calibrated" to remove the signature of trails in the dark images and other detector-related sources of noise[14,15] (also Ogaz et al. 2015). Transient hot pixels in the darks are the major source of this noise. The imperfectly corrected hot pixels end up generating the same pattern of residuals in all the images. With multiple exposures (>8), it is possible to self-calibrate out this pattern and regain ~20% in B_{F435W} depth. ACS undergoes a monthly annealing process in order to reduce the population of hot pixels. The structure of hot pixels in the darks is reset after the anneal, making the self-calibration software procedure less effective. Therefore, for later epochs of observations, we grouped the ACS/WFC B_{F435W} and V_{F606W} exposures in order to straddle

[14] www.stsci.edu/hst/acs/software/Selfcal
[15] blogs.stsci.edu/hstff/2013/05/24/calibration-is-in-the-works/

the planned ACS anneals. The total number of I_{F814W} exposures is large enough to be self-calibrated with the number of images taken on either side of the ACS anneals, and so they are interlaced with the B_{F435W} and V_{F606W} observations.

Dither pattern. To maximize the sensitivity of the *HST* Frontier Fields, especially toward the edges of the WFC3/IR images where strong magnification is predicted, each epoch of observations is constrained to a fixed *HST* roll angle with small dithers between exposures. The requirement of fixed roll angle means that every *HST* visit within an epoch is fine-guiding on the same pair of stars, and therefore intervisit dithering is highly effective.

To mitigate self-persistence between visits, we used an intervisit dither pattern that displaced any two given visits by >1 WFC3/IR pixel (∼0.″13) while still retaining overall compactness. This was achieved by generating 35 pseudorandom dither locations from a 2D Sobol sequence covering a six-pixel square (Sobol 1967). At the same time, pixel-phase dithering was achieved by modulating this six-pixel pattern by a secondary 35-element 2D Sobol sequence sampling over pixel phase. Pairings of ACS and WFC3 filters were carefully matched to visit-specific dither locations such that no filter had a pile-up of exposures in either absolute location or in pixel phase.

The *HST* dithering within the Frontier Fields visits, comprising four half-orbit exposures per filter, used the standard WFC3/IR "IR-DITHER-BLOB" (Dressel et al. 2016). This intravisit dither pattern had several attractive features, including good intravisit subpixel phase sampling for WFC3/IR, stepping across WFC3/IR "blobs" of reduced detector sensitivity McCullough et al. (2016), and stepping across the ACS/WFC CCD gap. This intravisit dither pattern is also sufficient to reject cosmic-ray impacts marring the four half-orbit ACS exposures. Because of the compactness of IR-DITHER-BLOB, we do not completely fill in in the WFC3/IR "deathstar"—a ∼6" circular region of bad pixels—nor do we dither over the WFC3/IR "wagon-wheel," an extended region on the right edge of the detector with low quantum efficiency and color-dependent structure, which is not corrected by the existing flat fields.

WFC3/IR persistence. Like other sensitive *HST* WFC3/IR programs, the Frontier Field observations are scheduled to minimize the impact of IR detector persistence from bright objects previously observed by other *HST* programs (e.g., "bad actors"; Long et al. 2013). Every Frontier Field exposure is visually inspected for data quality issues including persistence, and additional checks for persistence are done.[16] Most persistence impacts small regions of the detector and decays rapidly enough to affect only a few exposures, and therefore can be effectively masked out in the final stacked WFC3/IR images. However, early WFC3/IR observations of the MACSJ0416.1-2403 parallel field were severely impacted by scanned WFC3/IR grism observations of a bright star, for which persistence over ∼30% of the WFC3/IR detector was visible for >24 hr after the grism observations (Long et al. 2014). *HST* schedulers quickly responded by changing the following week's schedule to prevent a repetition of this sequence of programs. We triggered an *HST* Observation Problem Report (HOPR) to re-observe 10 orbits, and our input resulted in a change in the *HST* scheduling systems for the time buffer after such bad actors. Additional HOPRs were called in Cycle 23 to repeat persistence-affected observations for Abell S1063 (eight orbits) and Abell 370 (six orbits).

[16] https://archive.stsci.edu/prepds/persist/

5.2. HST Data Reduction

We briefly describe here the Frontier Fields *HST* data pipeline and resulting high-level science products. For more details about the *HST* Frontier Fields data reduction, please see A. M. Koekemoer et al. (2017, in preparation) and the data release readme files associated with each *HST* data set.

Every incoming exposure is visually inspected and flagged for artifacts, including satellite trails and asteroids, IR persistence, and IR time-variable sky within a few days of acquisition. Intermediate v0.5 stacked and drizzled image products are produced with standard archival retrievals, at scales of 30 and 60 mas pixel^{-1}, with major artifacts masked. The images are aligned with astrometric solutions based on previous *HST* and ground-based catalogs, initially compiled during the construction of the public Frontier Fields lensing models in summer 2013. Thus all MAST-hosted Frontier Fields lensing models and *HST* data products are aligned to the same astrometric grid.

The v1.0 "best effort" image products are released within several weeks of the completion of the observing epoch for each cluster/parallel field pair at a given orientation and camera configuration. These best-effort image products include the following improvements above the v0.5 releases:

1. reprocessing of all exposures using the most recent ACS and WFC3 calibration files (darks, flats, biases).
2. improved astrometric alignment between filters and cameras.
3. improved treatment of ACS/WFC bias destriping.
4. "self-calibration" applied to the ACS/WFC images to remove residual detector noise/artifacts, including correction for CTE in the darks.
5. masking of any new WFC3/IR "blobs" and additional sources of persistence.
6. correction for WFC3/IR time-variable sky in the ramp-fitting, which most strongly affects the F105W observations due to the He I emission but also impacts all IR filters when observing close to the bright Earth limb.
7. inclusion of *HST* imaging from other programs in the same filters in the stacked images to achieve maximum depths.

All these high-level science products are available for public retrieval at the Frontier Fields pages hosted at the STScI MAST Archive (10.17909/T9KK5N).

5.3. Spitzer *Observations*

In *Spitzer* Cycles 9, 10, and 11, all six Frontier Fields clusters were observed with IRAC channels 1 and 2 (3.6 and 4.5 μm) with Director's discretionary time (Figure 7, Table 3). Combined with archival data, the final images are expected to have nominal 5σ point-source sensitivities of 26.6 ABmag at 3.6 μm and 26.0 ABmag at 4.5 μm. However, contributions from confusion and the intracluster light may mean that the observations are less sensitive at the cluster core. Two of the clusters (MACS0717.5+3745 and MACS1149.5+2223) are in a previously approved *Spitzer* Cycle-9 program SURFSUP (PI M. Bradač, 90009), and two of the clusters (MACSJ0416.1-2403 and MACS0717.1.5+3745) were observed by the

Table 4
HST Exposure Times for CLASH, HFF MACSJ0416.1-2403, and HUDF[a]

Camera/Filter	CLASH	HFF	HFF-par.	HUDF
ACS/WFC F435W	2.0	55.0	45.7	152.4
ACS/WFC F606W	2.0	31.5	24.5	174.4
ACS/WFC F814W	4.0	129.9	106.0	50.8
WFC3/IR F105W	2.8	68.9	74.2	266.7
WFC3/IR F125W	2.5	37.2	34.2	112.5
WFC3/IR F140W	2.5	30.3	34.2	86.7
WFC3/IR F160W	5.0	73.0	74.2	236.1

Note.
[a] Exposure times for CLASH (Postman et al. 2012) and HFF observations of both MACSJ0416.1-2403 cluster field and its parallel field, and for HUDF (ACS: Illingworth et al. 2013; WFC3: Koekemoer et al. 2013). The unit is kiloseconds.

Cycle-8 program iCLASH (PI R. Bouwens, 80168). Due to conflicting constraints on roll angle with *HST* and *Spitzer*, the IRAC and *HST* fields of view could not be matched in position angle. Furthermore, to maximize the depth of these observations the observing windows were constrained to the epochs with the lowest background. As a result there are significant "flanking field" areas covered by IRAC to 25 hr depth around the main *HST* fields. For the reduced *Spitzer* data products, readme files, and additional information, please see P. Capak et al. (2017, in preparation) and irsa.ipac.caltech.edu/data/SPITZER/Frontier/.

6. Lensing Models and Predictions

In order to enable study of background lensed galaxies by a broad cross section of the extragalactic community, the *HST* Frontier Fields team has also supported the development and public release of lensing maps for each selected cluster. In particular, magnification estimates for the high-redshift lensed galaxies are critical for determining their intrinsic luminosities and estimating the faint end of the UV luminosity function. The initial lensing models were based on data taken *before* the Frontier Fields observing campaign to ensure that the community could make use of the Frontier Fields data as soon as possible (Table 4). Five independent teams (Bradač; Clusters As Telescopes, PI J.P. Kneib & P. Natarajan; A. Zitrin & J. Merten; K. Sharon; L. Williams), using a diversity of approaches (Bradač et al. 2005; LENSTOOL: Jullo & Kneib 2009; Zitrin et al. 2009; Merten et al. 2009; GRALE: Mohammed et al. 2014), coordinated to adopt the same input archival *HST* and ground-based data sets, the same redshifts, and multiple image identifications (Tables 4, 5). These models were made public on MAST prior to the *HST* Frontier Fields observations in autumn 2013.[17] The initial pre-FF model predictions for the galaxy numbers and volumes probed at high redshift are described in Coe et al. (2015).

However, these first pre-FF models have been rapidly superseded. The deep *HST* data have resulted in an unprecedented set of strong-lensed arcs and multiple images for constraining the cluster potentials (e.g., Jauzac et al. 2014, 2015; Lam et al. 2014; Diego et al. 2015, 2016; Wang et al. 2015; Kawamata et al. 2016), doubling or tripling the number of multiple images (Table 5, Figure 8). Subsequent observations with the GLASS *HST* WFC3/IR grism GO program (Schmidt et al. 2014; Treu et al. 2015; see 10.17909/T9KG60) and new ground-based spectroscopic campaigns have greatly increased the number and accuracy of the redshifts for the background lensed FF galaxies (Ebeling et al. 2014; Johnson et al. 2014; Richard et al. 2014; Balestra et al. 2015; Grillo et al. 2015; Hoag et al. 2016). The detection of a lensed SN Ia in MACSJ0416.1-2403 has also provided a strong constraint on its true magnification (Rodney et al. 2015). The discovery of the multiply imaged SN Refsdal in MACSJ1149.5+2223 (Kelly et al. 2015) sparked an independent coordinated effort to predict the time delays and reappearance of this supernova in another image of the host galaxy (Kelly et al. 2016; Treu et al. 2016; also Rodney et al. 2016).

The newly discovered arcs and new spectroscopic redshifts have been incorporated into updated HFF+ versions of the Abell 2744 and MACSJ0416.1-2403 lensing models (Table 5); many of these have $z_{\rm phot} > 3$ (see Figure 8 for a comparison of the arc redshift distributions adopted by the pre-HFF and new HFF+ lensing models; Cypriano et al. 2004; Okabe & Umetsu 2008; Zitrin et al. 2009; 2013; Okabe et al. 2010a, 2010b; Merten et al. 2011; Christensen et al. 2012; Mann & Ebeling 2012; Jauzac et al. 2014; Lam et al. 2014; Richard et al. 2014; Balestra et al. 2015; Diego et al. 2015; Grillo et al. 2015; Jauzac et al. 2015; Rodney et al. 2015; Wang et al. 2015; Kawamata et al. 2016). The incorporation of these new multiple image systems often results in a reduction in the statistical uncertainty in the galaxy magnifications for a given model. All of the public HFF lensing models provide a range of possible realizations from which the statistical uncertainty of a given model set may be calculated (typically 100 but no fewer than 30). We plot the cumulative distribution of the galaxy magnification uncertainties $\sigma(\mathrm{model})/\langle\mu(\mathrm{model})\rangle$, for the galaxies and photometric redshifts provided by the ASTRODEEP catalogs (Merlin et al. 2016; Castellano et al. 2016a) for Abell 2744 (Figure 9) and MACSJ0416.1-2403 (Figure 10). Generally, the statistical uncertainties are reduced for the models computed with the new HFF data sets, with more dramatic reductions for the methods that rely strongly upon the strong-lensing constraints. The parametric methods (CATS, Sharon, Zitrin, GLAFIC) report median statistical magnification errors of 0.2%–5%, while the non-parametric methods (Bradač Williams, Diego) report median statistical magnification errors of 2%–11% for the post-HFF calculations (green curves), versus 2%–22% and 2%–17% respectively for pre-HFF models (blue curves). (We note that the statistical errors for the MACSJ0416.1-2403 Bradač post-HFF models (Hoag et al. 2016) included additional uncertainties due to the photometric redshift uncertainties of the multiple images. These were not included in the pre-HFF Bradač model, and thus may explain why the post-HFF statistical errors are larger for this model.)

We also examine the systematic uncertainties associated with the different model approaches by computing the method-to-method standard deviations for the CATS, Sharon, Zitrin NFW, Williams, and Bradač "best" magnification values for each input galaxy (first panels in Figures 9, 10). This model subset was chosen because they encompass the same methodologies for both pre-HFF and HFF+ models. We find that the additional constraints from the HFF data have done little to reduce the variations in magnification values across methodologies. The median systematic magnification uncertainties are

[17] archive.stsci.edu/prepds/frontier/lensmodels/

Table 5
Frontier Field Lensing Models[a]

Team	Method	Parallel?	Version	Data[b]	Abell 2744	MACSJ0416.1	MACSJ0717	MACSJ1149.5	Abell S1063	Abell 370
CATS	LENSTOOL	no	1	pre-HFF	10/2013	12/2013	12/2013	12/2013	12/2013	12/2013
			2	HFF–	⋯	10/2014	⋯	⋯	⋯	⋯
			2.1	HFF–	9/2015	⋯	⋯	⋯	⋯	⋯
			2.2	HFF–	9/2015	⋯	⋯	⋯	⋯	⋯
			3	HFF+	9/2015	9/2015	⋯	⋯	⋯	⋯
			3.1	HFF+	9/2015	9/2015	⋯	⋯	⋯	⋯
Sharon	LENSTOOL	no	1	pre-HFF	10/2013	12/2013	12/2013	12/2013	12/2013	12/2013
			2	pre-HFF	5/2014	5/2014	⋯	⋯	⋯	⋯
			3	HFF+	9/2015	9/2015	⋯	⋯	⋯	⋯
Zitrin	NFW	no	1	pre-HFF	9/2013	9/2013	9/2013	9/2013	9/2013	9/2013
& Merten	LTM	no	1	pre-HFF	9/2013	9/2013	9/2013	9/2013	9/2013	9/2013
	LTM-G	no	1	pre-HFF	9/2013	9/2013	9/2013	9/2013	9/2013	9/2013
	WL	yes	1	pre-HFF	9/2013	9/2013	9/2013	9/2013	9/2013	9/2013
	NFW	no	3	HFF+	9/2015	9/2015	⋯	⋯	⋯	⋯
	LTM-G	no	3	HFF+	9/2015	9/2015	⋯	⋯	⋯	⋯
GLAFIC		no	1	HFF–	11/2014	⋯	⋯	⋯	⋯	⋯
			3	HFF+	2/2016	2/2016	⋯	⋯	⋯	⋯
			3	HFF–			2/2016	2/2016	⋯	⋯
Williams	GRALE	no	1	pre-HFF	9/2013	9/2013	9/2013	9/2013	9/2013	9/2013
			2	HFF–	⋯	10/2014	⋯	⋯	⋯	⋯
			3	HFF+	⋯	11/2015	⋯	⋯	⋯	⋯
			3.1	HFF+	11/2015	11/2015	⋯	⋯	⋯	⋯
Bradač		yes	1	pre-HFF	9/2013	9/2013	9/2013	9/2013	9/2013	9/2013
			2	HFF–	9/2015	⋯	⋯	⋯	⋯	⋯
Diego		no	3	HFF+	⋯	2/2016	⋯	⋯	⋯	⋯

Notes.
[a] See https://archive.stsci.edu/prepds/frontier/lensmodels/ for models; http://www.stsci.edu/hst/campaigns/frontier-fields/Lensing-Models for lensing primer and description of the different methods. *Bradač models:* Wang et al. (2015), Hoag et al. (2016), Bradač et al. (2005, 2009). *CATS models:* Jauzac et al. (2012, 2014), Richard et al. (2014), Jullo & Kneib (2009). *Diego models:* Diego et al. (2005, 2007, 2015). *GLAFIC models:* Ishigaki et al. (2015), Oguri (2010); *Zitrin & Merten models:* Merten et al. (2011, 2009), Zitrin et al. (2013, 2009). *Sharon models:* Johnson et al. (2014), Jullo et al. (2007). *Williams models:* Mohammed et al. (2014), Liesenborgs et al. (2006).
[b] Pre-HFF models were constructed prior to the FF observations with the coordinated input data; HFF– models were constructed with FF observations but without coordination between the teams; HFF+ models were constructed with FF observations with coordinated inputs between teams.

less than 26% for Abell 2744 and 15% for MACSJ0416.1-2403 for the post-HFF models.

Additional programs have sought to understand and improve the systematics inherent in the lensing models (e.g., Zitrin et al. 2015a; Harvey et al. 2016; Johnson & Sharon 2016; Meneghetti et al. 2016; Mohammed et al. 2016). Using two simulated Frontier Fields-like clusters and data sets, Meneghetti et al. (2016) study the systematic effects of the lensing modeling approaches used by the Frontier Fields lensing teams. They find that magnifications within the Einstein radii are well constrained, with the largest uncertainties in the magnifications arising near the critical curves and substructures, and best parametric results yielding uncertainties relative to the input simulation of ∼10% for true magnifications ∼3 and 30% for true magnifications ∼10. With this simulation, Johnson & Sharon (2016) explore the systematic errors of parametric LENSTOOL models (Jullo & Kneib 2009) as a function of the number of multiple image systems with and without spectroscopic redshifts. They find that increasing the number of multiple image systems to 20 improved the accuracy in the magnification estimates, but the accuracy was not improved beyond 2% for $N > 20$ systems. Rather, they find that for a fixed number of multiple images, increasing the fraction of systems with spectroscopic redshifts increased the accuracy of the magnification estimates without changing the precision. Given the small fraction of systems with spectroscopic redshifts for the current HFF multiple image systems (currently ∼15% for Abell 2744 and MACSJ0416.1; Table 5), we expect that additional improvements in the model accuracy could be made with additional spectroscopic follow-up.

The Frontier Fields lensing models will continue to be refined, as the HFF observing program proceeds through September 2016, new ancillary spectroscopic and weak-lensing data sets are acquired, and the modeling methods improve. This investment is critical for ensuring the Frontier Fields' legacy for *JWST* studies. To continue to provide the best models to the broader community, a renewed effort to update the existing lensing models and incorporate new FF and ancillary data began in May 2015 for Abell 2744 and MACSJ0416.1-2403 (Table 4). The resulting models were publicly released in autumn 2015. A second round of lensing coordination is set to begin in summer 2016, and will encompass the last four clusters. The delivery of MACSJ1149.5+2223 and MACSJ0717.5+3647 models is due in February 2017, with

Table 6
Frontier Field Multiply Imaged Galaxies[a]

Data[b]	Abell 2744	MACSJ0416.1	MACSJ0717.5	MACSJ1149.5	Abell S1063	Abell 370
pre-HFF[c]	17/52/2	17/47/7	14/45/5	12/35/3	14/41/5	11/34/3
HFF+[c]	38/111/5	68/182/11	…	…	…	…
HFF–[d]	…	…	60/173/8	36/108/16	52/120/11	…

Notes.
[a] The number of multiple image families, total number of multiple images, and number of spectroscopic redshifts are given for each cluster/model generation.
[b] Pre-HFF models were constructed prior to the FF observations with the coordinated input data; HFF– models were constructed with FF observations but without coordination between the teams; HFF+ models were constructed with FF observations with coordinated inputs between teams.
[c] A complete list of arc positions and redshifts are available for pre-HFF and HFF+ models in each model directory at archive.stsci.edu/prepds/frontier/lensmodels/
[d] We cite the GLAFIC public HFF– models multiple image image families, given in Kawamata et al. (2016) for MACSJ0717.5+3745 and MACSJ1149.5+2223, and the multiple image families of Diego et al. (2016) for Abell S1063. Coordinated HFF+ models have not yet been released for these clusters.

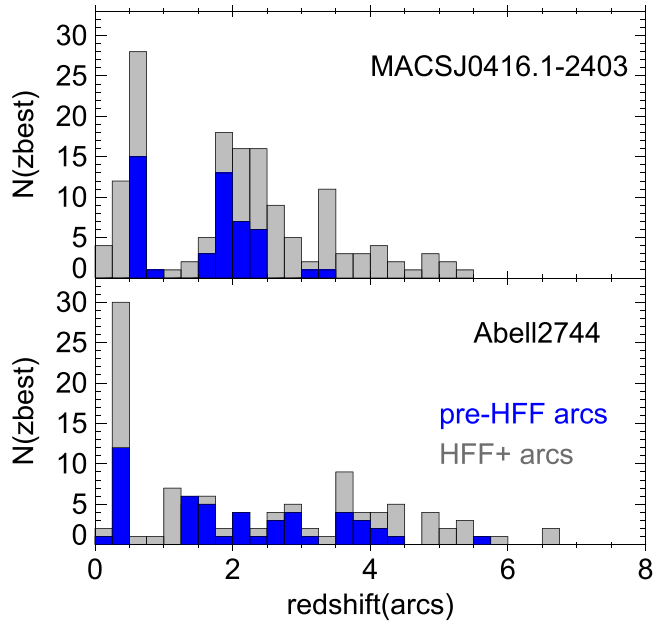

Figure 8. The redshift distributions for the multiple arc images used for the public Frontier Field lensing models for MACSJ0416.1-2403 and Abell 2744. Redshifts are drawn from the ASTRODEEP ZBEST catalog values (Castellano et al. 2016a and references therein). The pre-HFF arc redshifts are in blue, and the new HFF+ arc redshifts in gray.

final delivery of Abell S1063 and Abell 370 models due in September 2017.

7. Initial Results

In this section, we demonstrate the exceptional sensitivity of the Hubble Frontier Field images to faint and distant galaxies. We summarize the key early results from the current literature that address the primary goals of the HFF (Section 2), including the detection of new deep samples of intrinsically faint galaxy candidates during the epoch of reionization, dramatically improved constraints on the faint end of the UV luminosity function at $z > 6$, initial estimates of the sensitivity of the HFF as a function of stellar mass and star formation rates, and new understanding of the spatially resolved properties of distant HFF galaxies important for planning observations with *JWST*. We focus primarily on the studies of the first two Frontier Fields, Abell 2744 and MACSJ0416.1-2403, and make extensive use of the public ASTRODEEP multi-band photometric catalog and the catalog fitted to the spectral energy distribution (Castellano et al. 2016a; Merlin et al. 2016).

7.1. HST Detection Limits

The HFF v1.0 images of the first two clusters and their parallel fields have achieved the target depths presented in Table 2. Merlin et al. (2016) compute the 5σ detection limits for a point source within a $0\farcs4$ diameter aperture using the image rms values for these four sets of 60 mas pixel-scale images in the seven *HST* bands. These are 28.6–29.0 for B_{F435W}, 28.7–29.0 for V_{F606W}, 29.0–29.3 for I_{F814W}, 29.15–29.3 for Y_{F105W}, 28.8–29.0 for J_{F125W}, 28.9–29.1 for JH_{F140W}, and 29.0–29.1 for H_{F160W} (see Merlin et al. 2016, Table 1). We note that the total exposure times for these images are generally longer than that assumed in Table 2. The HFF program images were combined with archival *HST* data from the Dupke (11689), Siana (13389), Rodney (13386), and Postman (12459) programs when available. An additional 10 orbits of MACSJ0416.1-2403 (WFC3/IR: parallel, ACS/WFC: cluster) were reobserved due to severe persistence in the IR images.

We compare the 5σ detections of the HFF MACSJ0416.1-2403 cluster and parallel images to the CLASH MACSJ0416.1-2403 images, and the deepest available versions of the HUDF (ACS/WFC: Illingworth et al. 2013; WFC3/IR: Koekemoer et al. 2013) in Figures 11 and 12. The total exposure times for each filter and image are provided in Table 4. We plot the number counts as a function of AB magnitude measured within $0\farcs4$ diameter apertures for each of the *HST* bandpasses; these magnitudes are corrected for the expected flux loss within this aperture for a point source (-0.18 mag for B_{F435W}, V_{F606W}, -0.19 mag for I_{F814W}, -0.37 for Y_{F105W}, -0.42 J_{F125W}, -0.47 for JH_{F140W}, -0.48 for H_{F160W}). (Note that these number counts of the aperture magnitudes do not reflect the total magnitude number counts; refer to Merlin et al. 2016 for this analysis.)

The aperture photometry is computed with SExtractor v2.8.6 (Bertin & Arnouts 1996) in single-band mode, using a 1σ detection and analysis threshold and object deblending settings DEBLEND_NTHRESH = 64, DEBLEND_MINCONT = 0.0001. The images are convolved with a four-pixel Gaussian filter as part of the SExtractor detection. For the ACS images, we analyze the 30 mas pixel-scale images and the HFF self-calibrated versions and adopt DETECT_MINAREA = 50 pixels. For the WFC3 images, we analyze the 60 mas pixel-scale images and the HFF self-calibrated versions and adopt DETECT_MINAREA = 12.5 pixels. We use SExtractor for the background subtraction with BACKGROUND_SIZE set to 3.8 arcsec (128/64 pixels for 30/60 mas pixel scales), BACKGROUND_FILTERSIZE = 5, BACKPHOTO_TYPE = LOCAL, and the

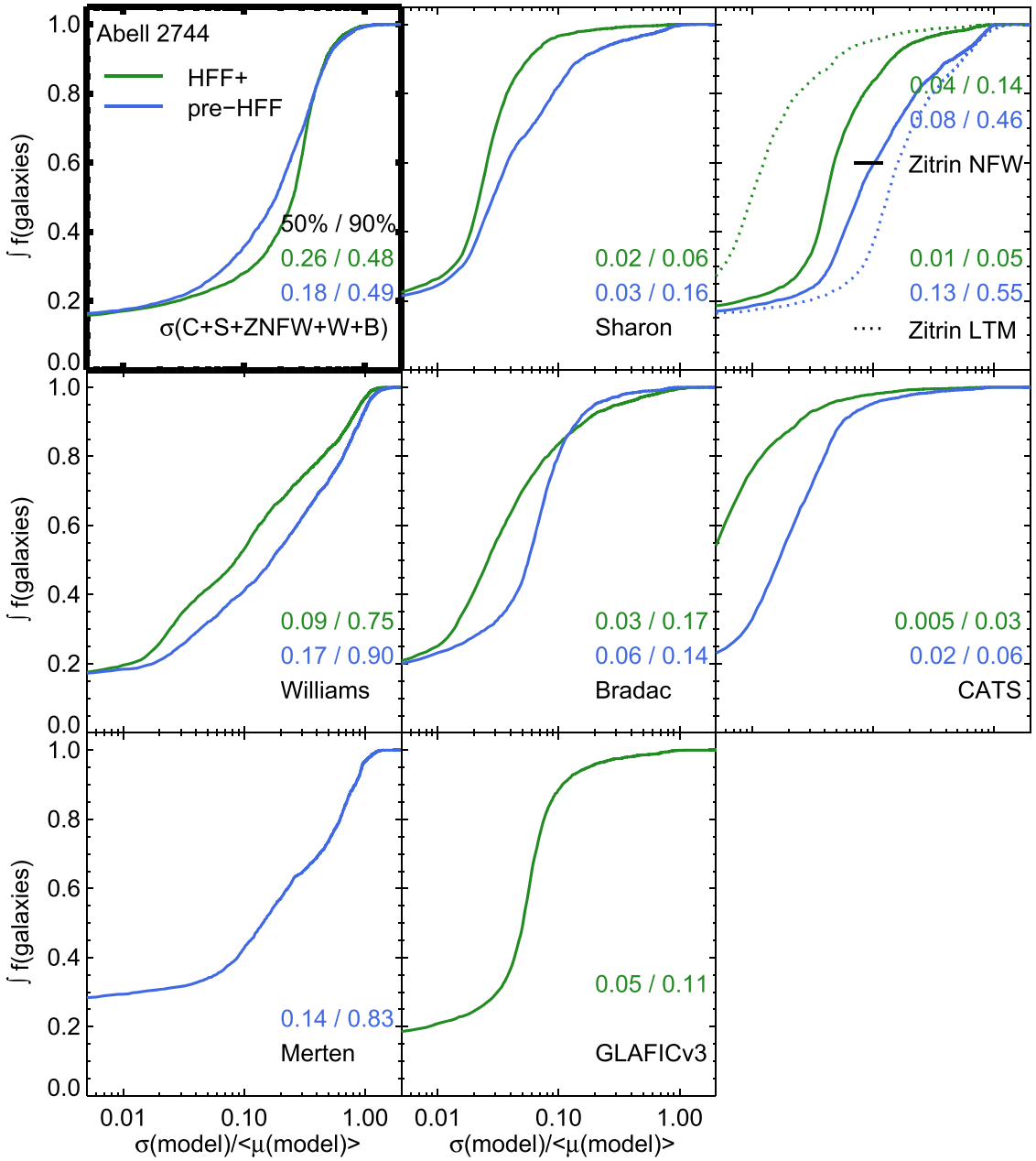

Figure 9. Cumulative distribution of the statistical uncertainties of each of the Frontier Fields models for Abell 2744 galaxies from the ASTRODEEP catalog (Castellano et al. 2016a; see Table 5 for full model lists). The standard deviation of the lensing model magnifications (σ(models)) is divided by the mean magnification for each galaxy/model set ($\langle\mu\,(\mathrm{model})\rangle$). Models created prior to the Frontier Field observations are shown in blue; models created using the HFF data and multiply imaged arcs are shown in green. For each model, we also give the value of $\sigma/\langle\mu\rangle$ at 50% and 90% cumulative distribution points. Finally, the first panel shows the systematic deviations for the first five sets of models (Sharon; Zitrin NFW; Williams; Bradač; CATS) created pre- and post-HFF observations.

annulus for the photometric background correction BACK-PHOTO_THICK = 1.44 arcsec (48/24 pixels for 30/60 mas pixel scales).

We find that the faint limit for 5σ detections is in good agreement with the target HFF depths (vertical dashed lines, Figures 11, 12). These are substantially deeper than the 1–2 orbit CLASH images, as expected given the factor of 10 difference in the exposure times. The HFF WFC3/IR images are ∼1 mag shallower than the HUDF12 WFC3/IR images; thus faint high-redshift HFF lensed galaxies require magnification factors >2.5 in order to probe intrinsic magnitudes fainter than unlensed galaxies in the HUDF12 images. The HFF ACS/WFC B_{F435W} images are slightly shallower (0.1–0.3 mag) than the HUDF ACS/WFC B_{F435W} image. The HFF ACS/WFC V_{F606W} images are ∼0.5 magnitudes shallower than the HUDF ACS/WFC V_{F606W} images. The HUDF ACS/WFC I_{F814W} image has less than half the exposure time of the HFF images, thus is ∼0.5 magnitudes shallower. The 5σ limits seen here in the number counts for the HUDF and MACSJ0416.1-2403 parallel fields are in good agreement with the 5σ depths reported in Finkelstein et al. (2015, Table 1).

For the cluster WFC3/IR images, there is evidence for lower detection rates than in the parallel field at $H_{F160W} \sim 28.5$ ABmag (first reported for Abell 2744 by Ishigaki et al. 2015, Figure 1). The completeness of object detections in the cluster fields is a strong function of the algorithms used to deblend the

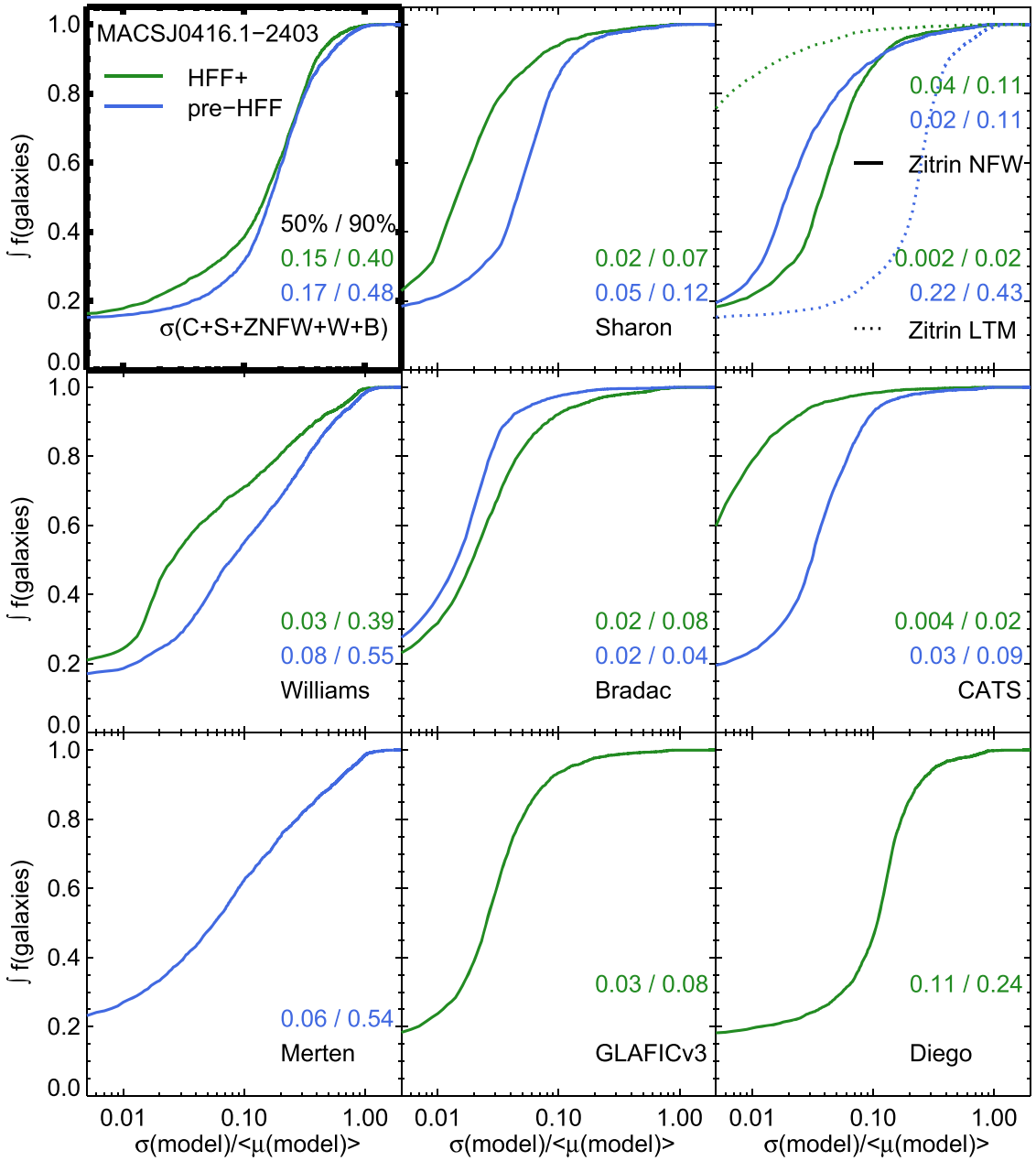

Figure 10. Same as Figure 9 but for MACSJ0416.1-2403: the cumulative distribution of the statistical uncertainties of each of the Frontier Fields models for MACSJ0416.1-2403 galaxies from the ASTRODEEP catalog (Castellano et al. 2016a; see Table 5 for full model lists). The first panel shows the systematic uncertainties for the first five sets of models (Sharon; Zitrin NFW; Williams; Bradač; CATS) created pre- and post-HFF observations.

cluster galaxies and correct for the intracluster light; the additional rms noise from the cluster also degrades the detection limit (see McLeod et al. 2016). Different groups have employed increasingly aggressive strategies to detect faint sources within the core of the HFF clusters. Early works (Atek et al. 2014; Ishigaki et al. 2015; Laporte et al. 2014; Zheng et al. 2014) used SExtractor for deblending, source detection, background correction, and galaxy photometry. In order to correct for the intracluster light, Oesch et al. (2014) subtracted a median-filter smoothed background image prior to SExtractor photometric calculations, and computed completeness estimates >60% for $H = 25$–28 high-redshift galaxies with magnification factors ⩽10. More recently, Merlin et al. (2016) have used the galaxy profile fitting software GALFIT (Peng et al. 2010) to subtract cluster galaxies and enable the detection of underlying faint sources, and to compute completeness efficiencies as a function of profile type (point source, disk, bulge) and magnitude, with 50% completeness at $H_{F160W} \sim 28.5$, 27.7, and 27.3 respectively. Finally, Livermore et al. (2017) have devised a wavelet approach that decomposes the images into Fourier modes and detects objects on the small spatial scales; this method is able to detect compact simulated galaxies to 28.5–29th magnitude at the 5σ level near the cores of Abell 2744 and MACSJ0416.1-2403 (Livermore et al. 2017; Figure 1).

7.2. High-redshift Galaxy Selection

The deep multiband *HST* and *Spitzer* imaging has enabled the selection of high-redshift galaxy candidates using both traditional Lyman break color–color selections and photometric

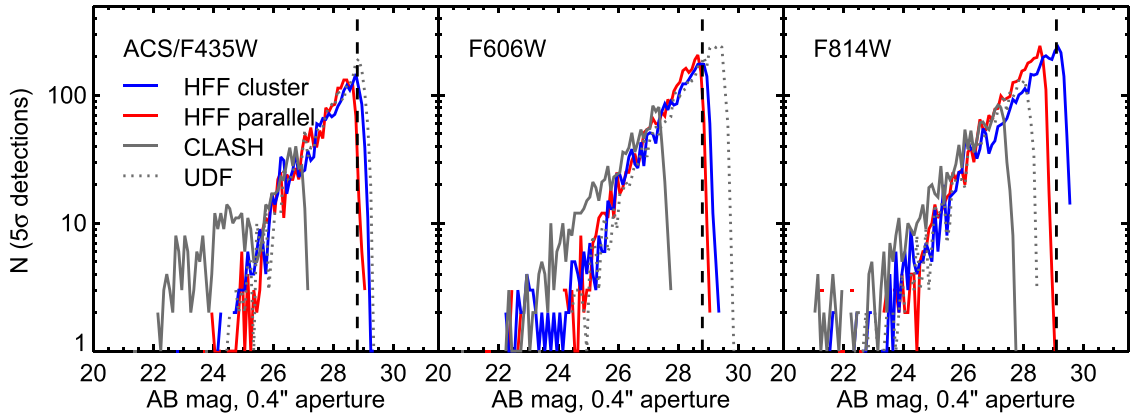

Figure 11. Number of 5σ detections as a function of AB magnitudes within a $0\farcs4$ diameter aperture for the *HST* ACS/WFC3 B_{F435W}, V_{F606W}, and I_{F814W} images. The magnitudes are corrected for the fraction of flux lost within the aperture, assuming a point source. The vertical dashed line gives the target HFF depths from Table 2.

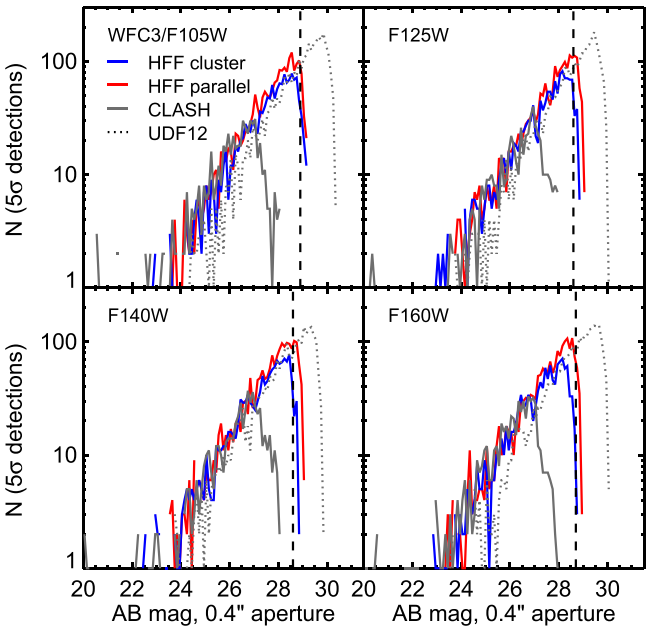

Figure 12. Number of 5σ detections as a function of AB magnitudes within a $0\farcs4$ diameter aperture for the *HST* WFC3/IR Y_{F105W}, J_{F125W}, JH_{F140W}, and H_{F160W} images. The magnitudes are corrected for the fraction of flux lost within the aperture, assuming a point source. The vertical dashed line gives the target HFF depths from Table 2.

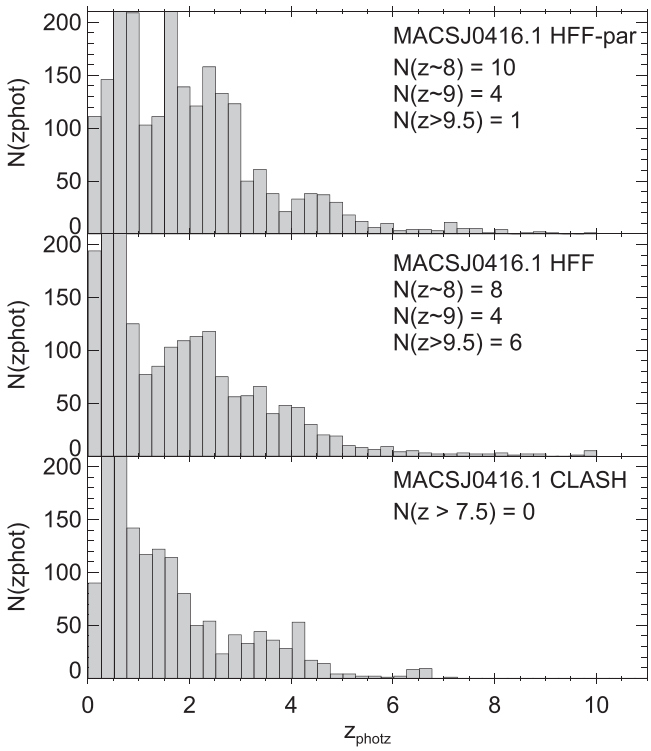

Figure 13. Photometric redshift distributions for the HFF MACSJ0416.1-2403 parallel field, HFF MACSJ0416.1-2403 cluster field from the ASTRODEEP catalog (Castellano et al. 2016a), and for the CLASH observations of MACSJ0416.1-2403 (Postman et al. 2012; Balestra et al. 2015; Grillo et al. 2015). Bradley et al. (2014) find one $z > 7.5$ candidate in the CLASH observations of MACSJ0416.1-2403, not reported by Castellano et al. (2016a).

redshift estimates. Uncertainties in the magnifications by the cluster do not affect the observed colors or the photometric redshift uncertainties. Castellano et al. (2016a) compute photometric redshifts using the full *HST*, *Spitzer*, and VLT Hawk-I *K*-band imaging for galaxies and report typical $\delta z/(1+z)$ errors of 4%, based on the available spectroscopic samples. In Figure 13, we show the photometric redshift distributions of the HFF MACSJ0416.1-2403 cluster and parallel field from Castellano et al. (2016a) versus the photometric redshift distributions computed from the CLASH observations of the MACSJ0416.1-2403 cluster (Postman et al. 2012; Balestra et al. 2015; Grillo et al. 2015; see also Castellano et al. 2016a, Figures 2 and 5). While CLASH detected one $z > 7.5$ candidate in the MACSJ0416.1-2403 cluster field (Bradley et al. 2014, not reported by Castellano et al. 2016a), the HFF observations find at least 18 $z > 7.5$ candidates.

The current numbers of galaxy candidates during the epoch of reionization ($6 < z < 10$) reported by various groups in the literature for MACSJ0416.1-2403 and Abell 2744 clusters and parallel fields are consistent with the predictions by Coe et al. (2015), using the pre-HFF lensing models (e.g., Atek et al. 2015; Finkelstein et al. 2015; Castellano et al. 2016b; Livermore et al. 2017; McLeod et al. 2016). The inclusion of the WFC3/IR JH_{F140W} has confirmed the detection of at least 33 $z > 8.5$ candidates in the first four Frontier Field cluster and parallel fields (e.g., McLeod et al. 2015, 2016). However, few

of the $z > 6$ HFF high-redshift candidates have been confirmed spectroscopically yet. The GLASS *HST* WFC3/IR grism observations report nine Lyα emitters at $z > 7$ in the HFF cluster fields (Schmidt et al. 2016). Ground-based observations have been more successful at detecting $z < 6$ lensed emission-line galaxies (e.g., Karman et al. 2017; Vanzella et al. 2016). Deep LBT observations have confirmed $z = 6.4$ Lyα emission for a multiply imaged, highly magnified $M_{UV} \sim -18.7$ system in MACSJ0717.5+3745 (Vanzella et al. 2014). However, deep Keck searches for C III] emission in Abell 2744 $z \sim 7$–8 have been unsuccessful thus far (e.g., Zitrin et al. 2015b); systematic follow-up of many high-redshift HFF candidates may require the capabilities of *JWST* and ALMA.

7.3. Intrinsically Faint Galaxy Populations at $z > 6$

The first goal of the Frontier Fields program to detect galaxies intrinsically fainter than any previously seen during the epoch of reionization has been achieved by a number of independent groups with the initial HFF observations. Most recently, Atek et al. (2015) and Livermore et al. (2017) measured rest-frame ultraviolet luminosity functions for Lyman break galaxies at $z \sim 6$, 7, 8 in the Abell 2744 and MACSJ0416.1-2403 cluster fields using lensing model magnifications computed with the HFF-based models described in Section 6. They find dozens of sources with intrinsic luminosities fainter than those reported for the HUDF ($M_{UV} \sim -17$; e.g., Finkelstein et al. 2015; Robertson et al. 2015), including galaxies more than 10 times intrinsically fainter than any previously reported. The best-fit UV luminosity functions from both studies are consistent and find $\alpha \sim -2.0$ and $M^*_{UV} = -20.7$ to –20.9. (Assuming smaller galaxy sizes results in higher completeness estimates and somewhat shallower α values; Oesch et al. 2014; Bouwens et al. 2016.) The faintest source reported by Atek et al. is -15.45 at $z \sim 7$, while Livermore et al. report lensed sources at -12.5 at $z \sim 6$, -14 at $z \sim 7$, and -15 at $z \sim 8$. Thus far, there is no evidence for a turnover in the $6 < z < 8$ rest-frame luminosity function at magnitudes brighter than $M_{UV} \sim -13$, placing the strongest limits yet on the number of faint galaxies contributing to the reionization of the universe (Castellano et al. 2016b; Livermore et al. 2017). The abundance of the faintest galaxies in the early universe also places strict constraints on the mass of a warm-dark-matter particle candiate at $\geqslant$2.1 keV (Menci et al. 2016).

The Frontier Fields have provided strong contraints on the total ultraviolet density $\rho_{\rm UV}$ and inferred global star formation density $\rho_{\rm SFR}$ at the earliest epochs visible to *HST* ($8 < z < 12$). Early analyses of Abell 2744 and the parallel field found several candidates at $z > 8$ (e.g., Ishigaki et al. 2014; Oesch et al. 2014; Zitrin et al. 2014). More recent studies including the first four HFF clusters and their parallel fields have found that the evolution in the ultraviolet luminosity density is consistent with a smooth linear transition from $z \sim 8$ to $z \sim 10$ (McLeod et al. 2016), in contrast to some previous works that claimed a break in the evolution of $\rho_{\rm UV}$ at $z > 8$ (e.g., Bouwens et al. 2012). Future studies of the remaining HFF fields will improve the statistical uncertainties at the faint end of the UV luminosity functions and cosmic star formation histories due to cosmic variances (Robertson et al. 2015).

Stellar mass and star formation rates derived for the Frontier Fields galaxy populations suggest that we are detecting the high-redshift progenitors of galaxies similar to the Milky Way and Local Group dwarfs for the first time. Castellano et al. (2016a) compute delensed stellar masses and star formation rates based upon the first two Frontier Fields multi-band photometry and the median magnification values given by the public pre-HFF lensing model (including galaxies in the parallel fields affected by weak lensing). They find that the HFF probes galaxies with stellar masses down to 10^6–$10^7\ M_\odot$ at $z < 9$, and star formation rates down to 0.1–1 $M_\odot\ {\rm yr}^{-1}$. These stellar masses are similar to those expected for the progenitors of the Large and Small Magellanic Clouds (Boylan-Kolchin et al. 2015). Independently, the deep *Spitzer* IRAC imaging from the SURFS-UP *Spitzer* imaging program combined with the Frontier Fields *HST*/*Spitzer* IRAC observations have detected 17 Lyman break galaxies at $6 < z < 10$ in MACSJ0717.5+3745 and MACSJ1149.5+2223, probing intrinsic stellar masses down to $2 \times 10^8\ M_\odot$ (Bradač et al. 2014; Huang et al. 2016).

Finally, HFF imaging of magnified galaxies has found that many of the high-redshift candidates have very compact sizes. Kawamata et al. (2015) measure the rest-frame UV half-light radii r_e between 0.08 and 0.8 kpc for a sample of ~40 $6 < z < 8$ galaxies in the Abell 2744 cluster and parallel field data. For galaxies with intrinsic luminosities brighter than $M_{UV} = -16.6$, they find that the size evolution scales as $r_e \propto (1+z)^{1.24\pm0.1}$, consistent with the disk formation models of Mo et al. (1998) and previous size estimates of $6 < z < 8$ galaxies (Oesch et al. 2007; Ono et al. 2013). Bouwen et al. (2016) examine galaxies at $2 < z < 8$ with the highest magnifications ($\mu = 10$–100) in the first four Frontier Fields clusters, and find that half-light radius scales $\propto L^{-0.5}$, such that galaxies fainter than $M_{UV} \sim -15$ may be as small as 20 pc. If true, then the completeness of the Frontier Field data to intrinsically faint high-redshift lensed galaxies is higher than previously assumed (e.g., Oesch et al. 2014; Atek et al. 2015; Livermore et al. 2017). Such compact sizes correspond to intrinsic angular sizes of ~4 mas, and thus can only be measured using *HST*/*JWST*/ALMA combined with strong lensing or with future 20–40 m class telescopes.

Very compact sizes and high star formation rates per unit area may be a necessary condition to produce UV escape fractions sufficient for faint galaxies to be the primary source of UV photons for reionization (e.g., Heckman et al. 2011; Borthakur et al. 2014; Alexandroff et al. 2015). Locally, high star formation rates per unit area are correlated with strong outflows, which in turn can create "leaky" environments for the UV photons. Assuming an SFR of $L_{UV} \sim 1.25 \times 10^{-28}\ M_\odot\ {\rm yr}^{-1}$ (Kennicutt 1998), an $M_{UV} = -15$ galaxy with UV size 20–50 pc implies SFR per unit area of >3–0.5 $M_\odot\ {\rm yr}^{-1}\ {\rm kpc}^{-2}$. This is comparable to the SFR per area found for local starbursts with UV-detected strong outflows (Heckman et al. 2015), but is lower than the SFR per area for the local compact analog of a Lyman break galaxy (~100 pc) with $f_{\rm esc} \sim 21\%$ reported by Borthakur et al. (2014).

8. Summary

We present the motivation and survey design for the Frontier Fields, a Director's discretionary time program with *HST* and *Spitzer* to see deeper into the distant universe than ever before. Six strong-lensing clusters and six parallel fields are observed, probing galaxies to observed optical/near-infrared magnitudes of ~29 ABmag and 10–100 times fainter in regions of high magnification. We explain the primary scientific goals of the Frontier Fields, the selection criteria for the fields, and the detailed properties of each Frontier Field cluster and parallel.

We describe the *HST* and *Spitzer* observing programs, and the coordinated Frontier Fields lensing model effort. We present the initial results from the first HFF observations, and demonstrate that the HFF is achieving its primary science goals regarding high-redshift galaxies.

The *HST* Frontier Fields observations of the last cluster (Abell 370) and its parallel field will be completed in September 2016, and the coordinated lensing models will be updated in 2017–2018. The full *Spitzer* Frontier Fields observations are complete and were publicly released in early 2016. The first Frontier Fields observations have already probed galaxies during the epoch of reionization to intrinsic luminosities fainter than any previously seen (e.g., Zitrin et al. 2014; Atek et al. 2015; Laporte 2015; Castellano et al. 2016; Livermore et al. 2017) and improved our statistical accounting of $z > 8$ galaxies (e.g., Kawamata et al. 2015; McLeod et al. 2015, 2016; Ishigaki et al. 2016). The full data set will place strong statistical constraints on the faint end of the luminosity function during this era (Robertson et al. 2015). At the time of publication of this article, over 80 refereed publications and four conferences have been devoted to or based in part on the Frontier Fields. These works include studies of high-redshift galaxies in the cluster and parallel fields, new cluster lensing models and dark-matter maps, supernovae/transient studies, studies of intracluster light and cluster evolution, and ancillary observations probing highly lensed background sources with major ground-based facilities. These data and associated models will provide a unique legacy for future studies of the high-redshift universe with the *JWST*.

The Frontier Fields program was initiated by STScI Director Dr. Matt Mountain using Director's discretionary time on the *Hubble Space Telescope*. We wish to acknowledge the Hubble Deep Fields Initiative science working group members for conceiving and recommending the Frontier Fields program: J. Bullock (chair), M. Dickinson, S. Finkelstein, A. Fontana, A. Hornschemeier Cardiff, J. Lotz, P. Natarajan, A. Pope, B. Robertson, B. Siana, J. Tumlinson, and M. Wood-Vasey. We also thank the mid-term Frontier Fields review committee for their service: J Bullock, M. Dickinson, R. Ellis, M. Kriek, S. Oey, S. Seitz, S. A. Stanford, and J. Tumlinson. We recognize the contributors to the current Frontier Field lensing models: M. Bradač, S. Allen, D. Applegate, B. Cain, A. Hoag, P. Kelly, P. Schneider, T. Schrabback, T. Treu, A. von der Linden, J.-P. Kneib, P. Natarajan, H. Ebeling, J. Richard, B. Clement, M. Jauzac, E. Jullo, M. Limousin, E. Egami, J. Merten, A. Zitrin, I. Balestra, M. Bartelmann, N. Benitez, A. Biviano, T. Broadhurst, M. Carrasco, D. Coe, N. Czakon, M. Donahue, T. Eichner, R. Ellis, C. Giocoli, S. Golwala, C. Grillo, O. Host, L. Infante, S. Jouvel, D. Lemze, A. Mercurio, E. Medezinski, P. Melchior, A. Molino, M. Meneghetti, A. Monna, J. Moustakas, L. Moustakas, T. Mroczkowski, M. Nonino, M. Okabe, M. Postman, J. Rhodes, P. Rosati, J. Sayers, S. Seitz, K. Umetsu, K. Sharon, T. Johnson, M. Bayliss, L. Wiliams, I. Mohammed, P. Saha, J. Liesenborgs, K. Sebesta, M. Ishigaki, R. Kawamata, M. Oguri, J. M. Diego, D. Lam, and J. Lim. Finally, we thank David Adler, George Chapman, Bill Workman, Ian Jordan, Alan Welty, Karen Levay, Scott Fleming, Brandon Lawton, Carol Christian, Tony Darnell, Frank Summers, Kathy Cordes, Bonnie Eisenhamer, Lisa Frattare, Ann Jenkins, Hussein Jirdeh, John Maple, Holly Ryer, Ray Villard, Tracy Vogel, and Donna Weaver for their contributions to the *HST* Frontier Fields effort. We acknowledge the ASTRODEEP team for their public Frontier Fields galaxy catalogs for Abell 2744, MACSJ0416.1-2403, and associated parallel fields.

Based on observations obtained with the NASA/ESA *Hubble Space Telescope*, retrieved from the Mikulski Archive for Space Telescopes (MAST) at the Space Telescope Science Institute (STScI). STScI is operated by the Association of Universities for Research in Astronomy, Inc. under NASA contract NAS 5-26555. This work is based in part on observations made with the *Spitzer Space Telescope*, which is operated by the Jet Propulsion Laboratory, California Institute of Technology under a contract with NASA. This work utilizes gravitational lensing models produced by PIs Bradač, Natarajan & Kneib (CATS), Merten & Zitrin, Sharon, Williams, and the GLAFIC and Diego groups. This lens modeling was partially funded by the *HST* Frontier Fields program conducted by STScI. We acknowledge ESO VIMOS CLASH-VLT Large Programme (186.A-0798, PI P. Rosati). Based on data collected at Subaru Telescope by PI K. Umetsu and archival imaging obtained from Subaru–Mitaka–Okayama–Kiso Archive (SMOKA), which is operated by the Astronomy Data Center, National Astronomical Observatory of Japan.

References

Abell, G. 1958, ApJS, 3, 211
Abell, G., Corwin, H. G., & Olowin, R. 1989, ApJS, 70, 1
Abraham, R., Tanvir, N. R., Santiago, B. X., et al. 1996, MNRAS, 279, 47
Alavi, A., Siana, B., Richard, J., et al. 2014, ApJ, 780, 143
Alavi, A., Siana, B., Richard, J., et al. 2016, ApJ, 832, 56
Alexandroff, R., Heckman, T. M., Borthakur, S., Overzier, R., & Leitherer, C. 2015, ApJ, 810, 104
Allen, S. W. 1998, MNRAS, 296, 392
Atek, H., Richard, J., Jauzac, M., et al. 2015, ApJ, 814, 69
Atek, H., Richard, J., Kneib, J.-P., et al. 2014, ApJ, 786, 60
Balestra, I., Mercurio, A., Sartoris, B., et al. 2016, ApJS, 224, 33
Balestra, I., Vanzella, E., Rosati, P., et al. 2013, A&A, 559, L9
Barger, A. J., Cowie, L. L., Mushotzky, R. F., et al. 2005, AJ, 129, 578
Beckwith, S., Stiavelli, M., Koekemoer, A., et al. 2006, AJ, 132, 1729
Behroozi, P., Wechsler, R., & Conroy, C. 2013, ApJ, 770, 57
Bertin, E., & Arnouts, S. 1996, A&AS, 117, 393
Bezecourt, J., Kneib, J. P., Soucail, G., & Ebbels, T. M. D. 1999a, A&A, 347, 21
Bezecourt, J., Soucail, G., Ellis, R. S., & Kneib, J. P. 1999b, A&A, 351, 433
Böhringer, H., Schuecker, P., Guzzo, L., et al. 2004, A&A, 425, 367
Boone, F., Clément, B., Richard, J., et al. 2013, A&A, 559, L1
Borthakur, S., Heckman, T., Leitherer, Cl., & Overzier, R. 2014, Sci, 346, 216
Boschin, W., Giarardi, M., Spolaor, M., & Barrena, R. 2006, A&A, 449, 461
Bouwens, R. J., Bradley, L., Zitrin, A., et al. 2014, ApJ, 795, 126
Bouwens, R. J., Illingworth, G. D., Franx, M., & Ford, H. 2007, ApJ, 670, 928
Bouwens, R. J., Illingworth, G. D., González, V., et al. 2010, ApJ, 725, 1587
Bouwens, R. J., Illingworth, G. D., Oesch, P. A., et al. 2012, ApJ, 754, 83
Bouwens, R. J., Illingworth, G. D., Oesch, P. A., et al. 2015a, ApJ, 803, 34
Bouwens, R. J., Illingworth, G. D., Oesch, P. A., Caruana, J., Holwerda, B., Smit, R., & Wilkins, S. 2015b, ApJ, 811, 140
Bouwens, R. J., Illingworth, G. D., Oesch, P. A., et al. 2016, ApJ, submitted (arXiV:1608.00966)
Bouwens, R. J., Illingworth, G. D., Rosati, P., et al. 2003, ApJ, 595, 589
Boylan-Kolchin, M., Bullock, J. S., & Garrison-Kimmel, S. 2014, MNRAS, 443, L44
Boylan-Kolchin, M., Weisz, D. R., Johnson, B. D., et al. 2015, MNRAS, 453, 1503
Bradač, M., Ryan, R., Casertano, S., et al. 2014, ApJ, 785, 108
Bradač, M., Schneider, P., Lombardi, M., & Erben, T. 2005, A&A, 437, 39
Bradač, M., Treu, T., Applegate, D., et al. 2009, ApJ, 706, 1201
Bradley, L. D., Trenti, M., Oesch, P. A., et al. 2012, ApJ, 760, 108
Bradley, L. D., Zitrin, A., Coe, D., et al. 2014, ApJ, 792, 76
Braglia, F., Pierini, D., & Bohringer, H. 2007, A&A, 470, 425
Brammer, G., Pirzkal, N., McCullough, P., & MacKenty, J. 2014, Instrument Science Report WFC3, Time-varying Excess Earth-glow Backgrounds in

the WFC3/IR Channel (Baltimore, MD: STScI), www.stsci.edu/hst/wfc3/documents/ISRs/WFC3-2014-03.pdf
Brammer, G., van Dokkum, P. G., Illingworth, G. D., et al. 2013, ApJ, 765, 2
Broadhurst, T., Umetsu, K., Medezinski, E., Oguri, M., & Rephaeli, Y. 2008, ApJ, 685, L9
Casertano, S., de Mello, D., Dickinson, M., et al. 2000, AJ, 120, 2747
Castellano, M., Amorín, R., Merlin, E., et al. 2016a, A&A, 590, 31
Castellano, M., Yue, B., Ferrara, A., et al. 2016b, ApJ, 823, 40
Christensen, L., Richard, J., Hjorth, J., et al. 2012, MNRAS, 427, 1953
Coe, D., Bradley, L., & Zitrin, A. 2015, ApJ, 800, 84
Coe, D., Zitrin, A., Carrasco, M., et al. 2013, ApJ, 762, 32
Cohen, J., Hogg, D. W., Blandford, R., et al. 2000, ApJ, 538, 29
Couch, W. J., & Newell, E. B. 1982, PASP, 94, 610
Cypriano, E. S., Sodre, L., Kneib, J.-P., & Campusano, L. E. 2004, ApJ, 613, 95
da Cunha, E., Walter, F., Decarli, R., et al. 2013, ApJ, 765, 9
Davis, M., Guhatharkurta, P., Konidaris, N. P., et al. 2007, ApJL, 660, 1
Dickinson, M. 1999, in AIP Conf. Proc. 470, A Complete NICMOS Map of the Hubble Deep Field North, ed. S. S. Holt & E. P. Smith (Melville, NY: AIP), 122
Dickinson, M., Papovich, C., Ferguson, H. C., & Budavái, T. 2003, ApJ, 587, 25
Diego, J. M., Broadhurst, T., Benitez, N., et al. 2015, MNRAS, 446, 683
Diego, J. M., Broadhurst, T., Wong, J., et al. 2016, MNRAS, 459, 3447
Diego, J. M., Protopapas, P., Sandvik, H. B., & Tegmark, M. 2005, MNRAS, 360, 477
Diego, J. M., Tegmark, M., Protopapas, P., & Sandvik, H. B. 2007, MNRAS, 375, 958
Dressel, L., et al. 2016, Wide Field Camera 3 Instrument Handbook, Version 8.0 (Baltimore, MD: STScI)
Ebeling, H., Barrett, E., & Donovan, D. 2004, ApJ, 609, L49
Ebeling, H., Barrett, E., Donovan, D., Ma, C.-. J., Edge, A. C., & van Speybroeck, L. 2007, ApJ, 661, L33
Ebeling, H., Edge, A. C., & Henry, J. P. , 2001, ApJ, 553, 668
Ebeling, H., Ma, C.-J., & Barrett, E. 2014, ApJS, 211, 21
Eckert, D., Jauzac, M., Shan, H., et al. 2015, Natur, 528, 105
Edge, A. C., Ebeling, H., Bremer, M., et al. 2003, MNRAS, 339, 913
Egami, E., Rawle, T. D., Pérez-González, P. G., et al. 2010, A&A, 518, L12
Ellis, R., McLure, R. J., Dunlop, J. S., et al. 2013, ApJ, 763, 7
Fan, X., Strauss, M. A., Becker, R. H., et al. 2006, AJ, 132, 117
Ferguson, H. C., Dickinson, M., & Williams, R. E. 2000, ARA&A, 38, 667
Fernádez-Soto, A., Lanzetta, K. M., & Yahil, A. 1999, ApJ, 513, 34
Finkelstein, S., Papovich, C., Giavalisco, M., et al. 2010, ApJ, 719, 1250
Finkelstein, S., Papovich, C., Salmon, B., et al. 2012, ApJ, 756, 164
Finkelstein, S., Ryan, R. E., Papovich, C., et al. 2015, ApJ, 810, 71
Fontana, A., Donnarumma, I., Vanzella, E., et al. 2003, ApJ, 594, 9
Fontana, A., Salimbeni, S., Grazian, A., et al. 2006, A&A, 459, 745
Ford, H., Bartko, F., Bely, P. Y., et al. 1998, SPIE, 3356, 234
Franx, M., Labbé, I., Rudnick, G., et al. 2003, ApJ, 587, 79
Giacconi, R., Rosati, P., Tozzi, P., et al. 2001, ApJ, 551, 624
Giavalisco, M., Dickinson, M., Ferguson, H. C., et al. 2004, ApJL, 600, L103
Giovannini, G., Tordi, M., & Feretti, L. 1999, NewA, 4, 141
Gómez, P. L., Valkonen, L. E., Romer, A., et al. 2012, AJ, 144, 79
Grazian, A., Fontana, A., de Santis, C., et al. 2006, A&A, 449, 951
Grillo, C., Karman, W., Suyu, S. H., et al. 2016, ApJ, 822, 78
Grillo, C., Suyu, S. H., Rosati, P., et al. 2015, ApJ, 800, 38
Grogin, N., Kocesvski, D. D., Faber, S. M., et al. 2011, ApJS, 197, 35
Gruen, D., Brimioulle, F., Seitz, S., et al. 2013, MNRAS, 432, 1455
Guhathakurta, P., Tyson, J. A., & Majewski, S. R. 1990, ApJ, 357, 9
Heckman, T., Alexandroff, R. A., Borthakur, S., Overzier, R., & Leitherer, C. 2015, ApJ, 809, 147
Heckman, T., Borthakur, S., Overzier, R., et al. 2011, ApJ, 730, 5
Hilbert, B. 2014, Instrument Science Report WFC3 2014-17, Updated non-linearity calibration method for WFC3/IR (Baltimore, MD: STSci), www.stsci.edu/hst/wfc3/documents/ISRs/WFC3-2014-17.pdf
Hinshaw, G., Larson, D., Komatsu, E., et al. 2013, ApJS, 208, 19
Hoag, A., Huang, K.-H., Treu, T., et al. 2016, ApJ, 831, 182
Hornschemeier, A., Brandt, W. N., Garmire, G. P., et al. 2000, ApJ, 541, 49
Huang, K.-H., Bradač, M., Lamaux, B. C., et al. 2016, ApJ, 817, 11
Illingworth, G. D., & Bouwens, R. 2010, in AIP Conf. Proc. 1294, The Cosmic Star Formation Rate Density since z 10: Constraints on Galaxies in the First Gyr, ed. D. J. Whalen, V. Bromm, & N. Yoshida (Melville, NY: AIP), 202
Illingworth, G. D., Magee, D., Oesch, P. A., et al. 2013, ApJS, 209, 6
Ishigaki, M., Kawamata, R., Ouchi, M., Oguri, M., Simasaku, K., & Ono, Y. 2015, ApJ, 799, 12
Ishigaki, M., Ouchi, M., & Harikane, Y. 2016, ApJ, 822, 5
Jauzac, M., Clément, B., Limousin, M., et al. 2014, MNRAS, 443, 1549
Jauzac, M., Jullo, E., Kneib, J.-P., et al. 2012, MNRAS, 426, 3369
Jauzac, M., Richard, J., Jullo, E., et al. 2015, MNRAS, 452, 1437
Johnson, T. L., Sharon, K., Bayliss, M. B., et al. 2014, ApJ, 797, 48
Johnson, T. L., & Sharon, K. 2016, ApJ, 832, 82
Jones, T. J., Wang, X., Schmidt, K. B., et al. 2015, AJ, 149, 107
Jullo, E., Kneib, J.-P., Limousin, M., et al. 2007, NJPh, 9, 447
Jullo, E., & Kneib, J. P. 2009, MNRAS, 395, 1319
Karman, W., Caputi, K. I., Grillo, C., et al. 2015, A&A, 574, A11
Karman, W., Caputi, K. I., Caminha, G. B., et al. 2017, A&A, 599, A28
Kartaltepe, J., Ebeling, H., Ma, C.-J., & Donovan, D. 2008, MNRAS, 389, 1240
Kawamata, R., Ishigaki, M., Shimasaku, K., Oguri, M., & Ouchi, M. 2015, ApJ, 804, 103
Kawamata, R., Oguri, M., Ishigaki, M., Shimasaku, K., & Ouchi, M. 2016, ApJ, 819, 114
Kempner, J. C., & David, L. P. 2004, MNRAS, 349, 385
Kneib, J.-P., Mellier, Y., Fort, B., & Mathez, G. 1993, A&A, 273, 367
Kneib, J.-P., & Natarajan, P. 2011, ARA&A, 19, 47
Kelly, P., Rodney, S. A., Treu, T., et al. 2015, Sci, 347, 1123
Kelly, P., Rodney, S. A, Treu, T., et al. 2016, ApJ, 819, L8
Kennicutt, R. 1998, ARA&A, 36, 189
Koekemoer, A. M., Ellis, R. S., McLure, R. J., et al. 2013, ApJS, 209, 3
Koekemoer, A. M., Faber, S. M., Ferguson, H. C., et al. 2011, ApJS, 197, 36
Labbé, I., González, V., Bouwens, R. J., et al. 2010, ApJ, 716, L103
Labbé, I., Oesch, P. A., Bouwens, R. J., et al. 2013, ApJ, 777, L19
Labbé, I., Rudnick, G., Franx, M., et al. 2003, ApJ, 591, 95
Lam, D., Broadhurst, T., Diego, J., et al. 2014, ApJ, 797, 98
Laporte, N., Streblyanska, A., Clement, B., et al. 2014, A&A, 562, L8
Laporte, N., Streblyanska, A., & Kim, S. 2015, A&A, 575, 92
Lawrence, A., Warren, S. J., Almani, O., et al. 2007, MNRAS, 379, 1599
Liesenborgs, J., De Rijcke, S., & Dejonghe, H. 2006, MNRAS, 367, 1209
Limousin, M., Ebeling, H., Richard, J., et al. 2012, A&A, 554, A71
Limousin, M., Richard, J., Jullo, E., et al. 2016, A&A, 588, 99
Livermore, R., Finkelstein, S., & Lotz, J. M. 2017, ApJ, 835, 113
Livermore, R., Jones, T., Richard, J., et al. 2012, MNRAS, 427, 688
Long, K. S., Baggett, S., & MacKenty, J. 2013, WFC3 Instrument Science Report 2013-07, Characterizing Persistence in the WFC3 IR Channel: Observations of Omega Cen (Baltimore, MD: STSci), www.stsci.edu/hst/wfc3/documents/ISRs/WFC3-2013-07.pdf
Long, K. S., Baggett, S. M., MacKenty, J., & McCullough, P. 2014, WFC3 Instrument Science Report 2014-14, Attempts to Mitigate Trapping Effects in Scanned Grism Observations of Exoplanet Transits with WFC3/IR (Baltimore, MD: STSci), www.stsci.edu/hst/wfc3/documents/ISRs/WFC3-2014-14.pdf
Lowenthal, J., Koo, D. C., Guzmán, R., et al. 1997, ApJ, 481, 673
Lutz, D., Poglitsch, A., Altieri, B., et al. 2011, A&A, 532, 90
MacKenty, J. W., Kimble, R. A., O'Connell, R. W., & Townsend, J. A. 2008, Proc. SPIE, 7010, 1
Madau, P., Ferguson, H. C., Dickinson, M. E., Giavalisco, M., Steidel, C., & Fruchter, A. 1996, MNRAS, 283, 1388
Mann, A. W., & Ebeling, H. 2012, MNRAS, 420, 2120
McCullough, P., Mack, J., Dulude, M., & Hilbert, B. 2016, Instrument Science Report WFC3 2014-21, Infrared Blobs: Time-dependent Flags, (Baltimore, MD: STSci), www.stsci.edu/hst/wfc3/documents/ISRs/WFC3-2014-21.pdf
McLeod, D. J., McLure, R. J., Dunlop, J. S., et al. 2015, MNRAS, 450, 3032
McLeod, D. J., McLure, R. J., & Dunlop, J. S. 2016, MNRAS, 459, 381
McLure, R. J., Dunlop, J. S., de Ravel, L., et al. 2011, MNRAS, 418, 2074
McPartland, C., Ebeling, H., Roediger, E., & Blumenthal, K. 2016, MNRAS, 455, 2994
Medenski, E., Umetsu, K., Nonino, M., et al. 2013, ApJ, 777, 42
Menanteau, F., Hughes, J. P., Sifón, C., et al. 2012, ApJ, 748, 7
Meneghetti, M., Natarajan, P., Coe, D., et al. 2016, MNRAS, submitted, (arXiv:1606.04548)
Menci, N., Grazian, A., Castellano, M., & Sanchez, N. G. 2016, ApJ, 825, 1
Merlin, E., Amorín, R., Castellano, M., et al. 2016, A&A, 590, 30
Merten, J., Cacciato, M., Meneghetti, M., Mignone, C., & Bartelmann, M. 2009, A&A, 500, 681
Merten, J., Coe, D., Dupke, R., et al. 2011, MNRAS, 417, 333
Mitra, S., Choudhury, T. R., & Ferrara, A. 2015, MNRAS, 454, 76
Mo, H. J., Mao, S., & White, S. D. M. 1998, MNRAS, 295, 319
Mobasher, B., Idzi, R., Benítez, N., et al. 2004, ApJ, 600, 167
Mohammed, I., Liesenborgs, J., Saha, P., & Williams, L. L. R. 2014, MNRAS, 439, 2651
Mohammed, I., Saha, P., Williams, L., Liesenborgs, J., & Sebesta, K. 2016, MNRAS, 459, 1698

Monna, A., Seitz, S., Greisel, N., et al. 2014, MNRAS, 438, 1417
Montes, M., & Trujillo, I. 2014, ApJ, 794, 137
Morandi, A., Ettori, S., & Mascardini, L. 2007, MNRAS, 379, 518
Oesch, P., Bouwens, R. J., Carollo, C. M., et al. 2010, ApJL, 709, 21
Oesch, P., Bouwens, R. J., Illingworth, G. D., et al. 2012, ApJ, 745, 110
Oesch, P., Bouwens, R. J., Illingworth, G. D., et al. 2013, ApJ, 773, 75
Oesch, P., Bouwens, R. J., Illingworth, G. D., et al. 2014, ApJ, 786, 108
Oesch, P., Brammer, G., van Dokkum, P. G., et al. 2016, ApJ, 819, 129
Oesch, P., Stiavelli, M., Carollo, C. M., et al. 2007, ApJ, 671, 1212
Ogaz, S., Avila, R., & Hilbert, B. 2015, STScI Newsletter, Vol. 32, blogs.stsci.edu/newsletter/files/2015/03/FFCalibration.pdf
Ogrean, G., van Weeren, R. J., Jones, C., et al. 2015, ApJ, 812, 153
Oguri, M. 2010, PASJ, 62, 1017
Okabe, N., Okura, Y., & Futamase, T. 2010, ApJ, 713, 291
Okabe, N., Takada, M., Umetsu, K., Futamase, T., & Smith, G. P. 2010, PASJ, 62, 811
Okabe, N., & Umetsu, K. 2008, PASJ, 60, 345
Oliver, S. J., Bock, J., Altieri, B., et al. 2012, MNRAS, 424, 1614
Ono, Y., Ouchi, M., Curtis-Lake, E., et al. 2013, ApJ, 777, 155
Owers, M. S., Randall, S. W., Nulsen, P. E. J., et al. 2011, ApJ, 728, 27
Paczynski, B. 1987, Natur, 325, 572
Papovich, C., Dickinson, M., & Ferguson, H. C. 2001, ApJ, 559, 620
Peng, C. Y., Ho, L., Impey, C. D., & Rix, H. W. 2010, AJ, 139, 2097
Pirzkal, N., Rothberg, B., Ryan, R., et al. 2013, ApJ, 775, 48
Planck Collaboration, Adam, R., Aghanim, N., et al. 2016, A&A, 596, 108
Pope, A., et al. 2016, ApJ, submitted
Pope, A., Scott, D., Dickinson, M., et al. 2006, MNRAS, 370, 1185
Postman, M., Coe, D., Benítex, N., Bradley, L., et al. 2012, ApJS, 199, 25
Rawle, T., Altieri, B., Egami, E., et al. 2016, MNRAS, 459, 1626
Richard, J., Kneib, J.-P., Limousin, M., Edge, A., & Jullo, E. 2010, MNRAS, 402, 44
Richard, J., Jauzac, M., Limousin, M., et al. 2014, MNRAS, 444, 268
Riess, A. G., Nugent, P. E., Gilliland, R. L., et al. 2001, ApJ, 560, 49
Riess, A. G., Strolger, L.-G., Tonry, J., et al. 2004a, ApJ, 600, L163
Riess, A. G., Strolger, L.-G., Tonry, J., et al. 2004b, ApJ, 607, 665
Rix, H.-W., Barden, M., Beckwith, S., et al. 2004, ApJS, 152, 163
Robberto, M. 2014, Proc SPIE, 9143, 91433Z
Robertson, B., Ellis, R. S., Dunlop, J. S., et al. 2014, ApJ, 796, 27
Robertson, B., Ellis, R., Furlanetto, S. R., & Dunlop, J. 2015, ApJ, 802, 19
Rodney, S., Patel, B., Scolnic, D., et al. 2015, ApJ, 811, 70
Rodney, S., Strolger, L.-G., Kelly, P. L., et al. 2016, ApJ, 820, 50
Schrimer, M., Carrasco, E. R., Garrel, V., et al. 2015, ApJS, 217, 33
Schlafly, E. F., & Finkbeiner, D. 2011, ApJ, 737, 103
Schlegel, D., Finkbeiner, D., & Davis, M. 1998, ApJ, 500, 525
Schmidt, K. B., Treu, T., Brammer, G., et al. 2014, ApJ, 782, L36
Schmidt, K., Treu, T., Bradač, M., et al. 2016, ApJ, 818, 38
Scoville, N., Abraham, R. G., Aussel, H., et al. 2007, ApJS, 172, 38
Smail, I., Dressler, A., Kneib, J. P., et al. 1996, ApJ, 469, 508
Smith, G. P., Ebeling, H., Limousin, M., et al. 2009, ApJ, 707, 163
Sobol, I. M. 1967, U.S.S.R Comput. Maths. Math. Phys., 7, 112
Songaila, A., Cowie, L. L., & Lilly, S. J. 1990, ApJ, 348, 371
Soucail, G., Fort, B., Mellier, Y., & Picat, J. P. 1987, A&A, 172, L14
Spergel, D., Verde, L., Peiris, H., et al. 2003, ApJS, 148, 175
Steidel, C., Giavalisco, M., Dickinson, M., & Adelberger, K. L. 1996, AJ, 112, 352
Stiavelli, M., Treu, T., Carollo, C. M., et al. 1999, A&A, 343, 25
Struble, M. F., & Rood, H. J. 1999, ApJS, 125, 35
Thompson, R. 2003, ApJ, 596, 748
Thompson, R. I., Illingworth, G. D., Bouwens, R., et al. 2005, AJ, 130, 1
Thompson, R., Storrie-Lombari, L. J., Weymann, et al. 1999, AJ, 117, 17
Treister, E., Urry, C. M., Chatzichristou, E., et al. 2004, ApJ, 616, 123
Treu, T., Schmidt, K., Brammer, G. B., et al. 2015, ApJ, 812, 114
Umetsu, K., Broadhurst, T., Zitrin, A., et al. 2011, ApJ, 738, 41
van Weeren, R. J., Röttgering, H. J., Brüggen, & Cohen, A. 2009, A&A, 505, 991
Vanzella, E., Barros, S., Cupani, G., et al. 2016, ApJ, 821, 27
Vanzella, E., Fontana, A., Zitrin, A., et al. 2014, ApJ, 783, 12
Wang, X., Hoag, A., Huang, K.-H., et al. 2015, ApJ, 811, 29
Windhorst, R. A., Cohen, S. H., Hathi, N. P., et al. 2011, ApJS, 193, 27
Williams, R. E., et al. 2000, AJ, 120, 2735
Williams, R. E., Blacker, B., Dickinson, M., et al. 1996, AJ, 112, 1335
Williamson, R. E., Baum, S., Bergeron, L. E., et al. 2011, ApJ, 738, 139
Yan, H., Yan, L., Zamojski, M. A., et al. 2011, ApJ, 728, 22
Zheng, W., Postman, M., Zitrin, A., et al. 2012, Natur, 489, 406
Zheng, W., Shu, X., Moustakas, J., et al. 2014, ApJ, 795, 93
Zitrin, A., Broadhurst, T., Rephaeli, Y., & Sadeh, S. 2009, ApJ, 707, L102
Zitrin, A., & Broadhurst, T. 2009, ApJ, 703, L132
Zitrin, A., Ellis, R., Belli, S., & Stark, D. P. 2015b, ApJ, 805, 44
Zitrin, A., Fabris, A., Merten, J., et al. 2015a, ApJ, 801, 44
Zitrin, A., Meneghetti, M., Umetsu, K., et al. 2013, ApJ, 762, L30
Zitrin, A., Zheng, W., Broadhurst, T., et al. 2014, ApJL, 793, 12